Journal of Manufacturing Processes 134 (2025) 558–588

Contents lists available at ScienceDirect

Journal of Manufacturing Processes

journal homepage: www.elsevier.com/locate/manpro

Review article

Eddy current testing and monitoring in metal additive manufacturing: A review

Medad C.C. Monu *, Josiah C. Chekotu, Dermot Brabazon

I-Form, Advanced Manufacturing Research Centre, Dublin City University, Glasnevin, Dublin 9, Ireland
Advanced Processing Technology Research Centre, Dublin City University, Glasnevin, Dublin 9, Ireland
School of Mechanical and Manufacturing Engineering, Dublin City University, Glasnevin, Dublin 9, Ireland

ARTICLE INFO

Keywords
Eddy current testing
In-situ monitoring
Additive manufacturing
Non-destructive testing
Metal AM part quality

ABSTRACT

In-situ process monitoring and sensing play an indispensable role in ensuring the quality and repeatability of additively manufactured components, as well as providing a means for optimizing process parameters and increasing the uptime of additive manufacturing (AM) equipment. This review paper offers an overview of the current state-of-the-art in *ex-situ* and *in-situ* assessments of AM part quality using the eddy current-based non-destructive testing technique. The adoption of eddy current testing (ECT) for both *ex-situ* and *in-situ* AM assessments is still in its infancy. This review paper begins by providing a concise description of the ECT technique and parameters using select case studies on conventionally manufactured components. The implementation of ECT for metal AM part quality assessment is discussed using case studies on powder bed fusion, direct energy deposition, and subtractive/additive hybrid AM components. Additionally, this paper presents the challenges and requirements for further development in this area towards developing closed-loop smart control and AM digital twins. These advancements hold the key to unlocking the full potential of metal AM techniques, thereby enabling more efficient and sustainable manufacturing practices.

1. Introduction

Additive manufacturing (AM), commonly known as 3D printing, has emerged as a transformative technology with the potential to revolutionize various industries ranging from aerospace and automotive to healthcare and electronics. In metal AM processes, such as powder bed fusion (PBF) and directed energy deposition (DED), intricate components are built layer by layer from metal powder or wire feedstock using a laser or electron beam. According to ISO/ASTM 52900: 2021 standard [1], metal powder bed fusion using a laser beam is abbreviated as PBF-LB/M and as PBF-EB/M when an electron beam is used to melt the powder. In this review article, the PBF-LB and PBF-EB abbreviations will be used for easy readability, whilst PBF refers to both electron and laser-beam-based metal AM processes.

The greater parametric flexibility offered by PBF implies that the properties of the manufactured AM components such as physical, microstructural, and mechanical properties can be tailor-made to suit the desired application by simply adopting an optimized set of process parameters. However, the PBF process is inherently complex, characterized by stochastic physical phenomena influenced by 130 or more distinct process parameters [2,3]. To address this complexity, energy density (ED) in eq. (1) [4], serves as a design metric aimed at reducing the multitude of process parameters to a manageable and practical number, that is thermodynamically resolvable to some extent.

$$ED = \frac{P}{f(V, f, H, L)} \tag{1}$$

In eq. (1) the terms *P, V,* and *f* represent the laser power (Watts), scan velocity (mm/s), and the size of the laser (PBF-LB) or electron (PBF-EB) beam's focal spot (μm), respectively. *H,* the hatch distance, denotes the distance (mm) between successive passes of the beam within the same layer, and *L* represents the layer thickness (mm) of the deposited powder.

Regardless of the selected process parameters, the PBF-LB process is characterized by high melt pool temperatures (peak temperatures) due to electron/laser irradiation [5]. The process is also associated with processing chamber pressures exceeding 50 mbar above ambient atmosphere [6], cooling gradients larger than 10^7 K/m, and cooling rates of the order of 10^7 K/s considering a typical laser scan speed of the order of 1000 mm/s [7,8]. In PBF-LB, there is also the convective cooling

* Corresponding author at: I-Form, Advanced Manufacturing Research Centre, Dublin City University, Glasnevin, Dublin 9, Ireland.
E-mail address: medad.monu2@mail.dcu.ie (M.C.C. Monu).

https://doi.org/10.1016/j.jmapro.2024.12.033
Received 11 September 2024; Received in revised form 2 December 2024; Accepted 17 December 2024
Available online 6 January 2025
1526-6125/© 2024 The Authors. Published by Elsevier Ltd on behalf of The Society of Manufacturing Engineers. This is an open access article under the CC BY license (http://creativecommons.org/licenses/by/4.0/).

effect from the purging gas. These conditions often result in defects such as keyhole porosities, lack of fusion defects, liquation cracks (hot cracking), warpage, delamination, spatter, balling, and high surface roughness. Optimization of process parameters is therefore necessary to avoid/reduce the aforementioned defects, which can be done through conventional trial and error methods. However, this method involves costly, laborious, and time-consuming destructive characterization, documentation, and remanufacturing. Consequently, both human and machine resources can be significantly taxed.

While metal AM offers unparalleled design flexibility and reduced lead times, improving the methods for quality and integrity assessment of manufactured parts remains a critical challenge. As a result, there is a growing emphasis on rapid non-destructive testing (NDT) for already manufactured AM parts, and *in-situ* monitoring during the manufacturing process. The general form factor of commercially available PBF and DED machines now facilitates the incorporation of various *in-situ* monitoring and sensing approaches.

Among the array of NDT techniques used for quality assurance, eddy current testing (ECT) shows strong potential in metal AM. The ECT technique is based on the principle of electromagnetic induction. It involves inducing eddy currents in a conductive material using an alternating magnetic field generated by a coil probe. Changes in the material properties, such as conductivity and permeability, due to defects or variations in microstructure, alter the eddy current distribution, allowing for the detection and characterization of defects in the tested component. The advantages of ECT include high sensitivity to surface defects, the ability to detect defects through different layers, a quick and simple inspection process, measurement of material conductivity, capability to measure nonconductive coatings, portability, automation of equipment, contactless inspection, and faster inspection time with eddy current array technology. ECT is also recognized as a versatile, high-precision NDT, with rapid inspection capabilities, and cost-effectiveness [9]. These advantages feature ECT as a valuable and highly adaptable NDT method in various industries and application areas.

However, the detection accuracy of ECT is cross-sensitive to the materials' properties upon which it relies for defect detection and/or other material properties assessments. More specifically, the magnetic permeability of the material, its electrical conductivity, excitation frequency, lift-off, temperature, and the thickness of the part, all affect the overall performance and response to measure specific features such as inclusions, microstructure, cracks, porosity, lack of fusion, voids, and residual stresses. Nonetheless, these factors can be parameterized and optimized for specific use cases, as evidenced by existing literature on ECT applications in conventionally manufactured components such as welded pipe integrity and corrosion in coated metal structures [10–12].

Therefore, this review article comprehensively explores the application of eddy current monitoring and testing in the context of metal AM. Currently, there is a lack of published literature on the use of eddy current for assessing metal AM components. Hence, this article presents the first comprehensive survey of what is known about the use of ECT for post-process (*ex-situ*) assessment in metal AM, as well as the first review covering *in-situ* AM monitoring utilizing ECT technology. Given that ECT is a relatively new monitoring technique in the metal AM community, especially when compared to more common methods like thermal imaging, optical imaging, and infrared (IR) pyrometry monitoring, this review begins by explaining the fundamental principles and parameters of ECT in **Section 2,** using selected case studies of conventionally manufactured metal components and metal AM components where available. **Section 3** presents case studies highlighting the adaptation of ECT specifically for assessing metal AM components, while **Section 4** delves into recent advancements and case studies pertaining to *in-situ* monitoring in various metal AM techniques using ECT. Following this, **Section 5** presents the challenges and opportunities associated with integrating ECT into metal AM processes. By synthesizing existing literature and identifying gaps in knowledge, this review seeks to guide future research directions and foster the adoption of *in-situ* eddy current monitoring and sensing for enhanced quality control and process optimization in metal AM manufacturing.

2. Key factors in eddy current testing (ECT) and their effects

Compared to other *in-situ* AM monitoring techniques, ECT has the advantage of being a standardized NDT technique that can provide compliant part certificates and post-process inspection according to existing standards such as ASTME3166–20 [13] and others [14–37]. ECT can be used to identify microstructure evolution [38], detect volumetric discontinuities, and residual stress formations [39,40], in a large variety of ferromagnetic and non-ferromagnetic conductive materials [41]. ECT technology is based on Faraday's law of electromagnetic induction, which describes the interaction between a magnetic field source and test material. This interaction results in the generation of eddy currents within the test piece, the flow path of which is perturbed by the presence of cracks/porosities, microstructural inhomogeneity, or changes in geometry [42]. These perturbations appear as localized magnetic anomalies, detected as alterations in the measured coil electrical current phase, amplitude, and temporal magnitude when the component is scanned. This is schematically illustrated in Fig. 1(a - b). A typical ECT system comprises an oscillator, an excitation coil, a sense coil or array of coils, signal processing circuitry, and a data interpretation display. Relevant factors and their influence during ECT are described hereafter.

2.1. Skin depth or standard penetration depth, δ

The standard depth of penetration (meters) during ECT is a direct consequence of the skin effect phenomena [43]. This is expressed by eq. (2) where f represents excitation frequency (Hz), $\sigma_{\%IACS}$ is the conductivity of the material, μ_0 is the permeability of vacuum or free space of approximately $4\pi \times 10^{-7}$H/m or 1.2566×10^{-6} N·A^{-2}, and μ is magnetic permeability.

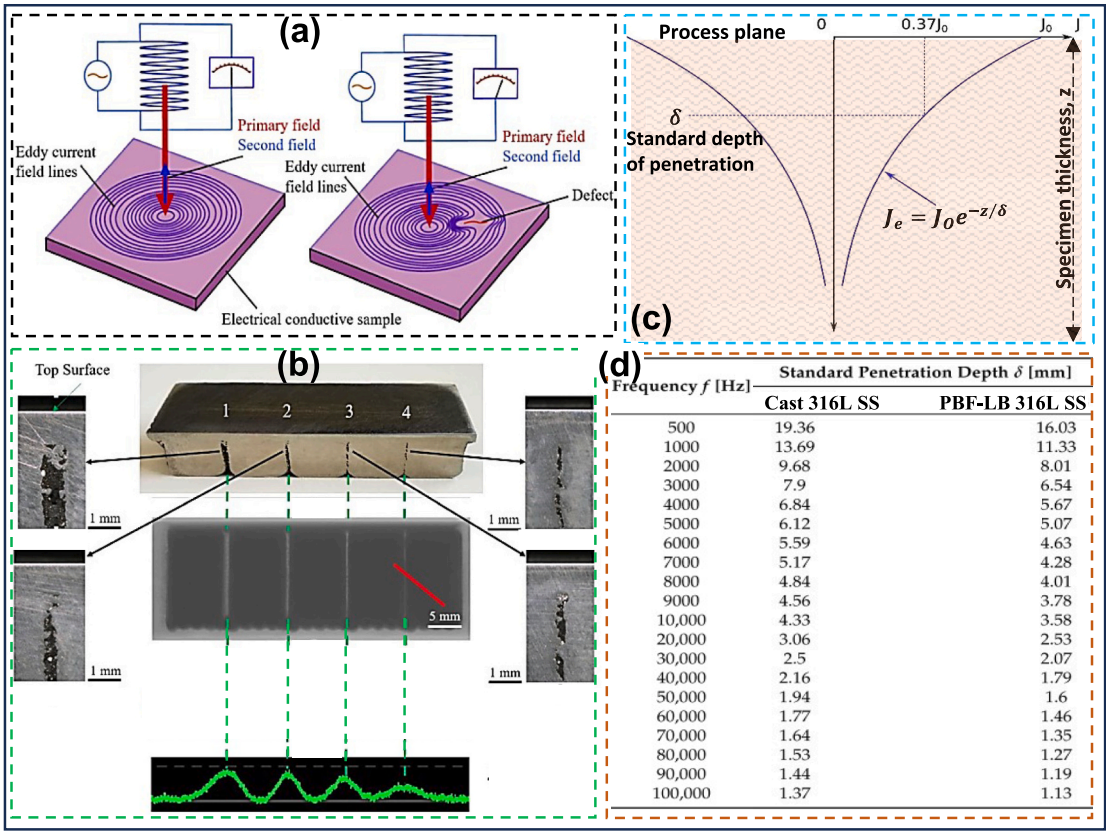
$$\delta = \sqrt{{}^{1}/_{\pi f \mu_o \mu \sigma_{IACS}}} \tag{2}$$

This standard depth of penetration defines the skin depth from the process plane (*i.e.*, the surface of the material under examination) at which the eddy current density, $\boldsymbol{J_e}$ decays by 1/e (*i.e.*, 37 %) of its surface value (refer to **Fig. 1**c) [44]. In practice, the eddy current density drops below 0.7 % of the surface value after approximately five skin depths [45]. As the skin depth increases, the ability to detect volumetric discontinuities in the material diminishes due to the associated decrease in eddy current density, $\boldsymbol{J_e}$.

The study conducted by García-Martí et al., [42] highlights how the standard depth of penetration can vary depending on the manufacturing techniques, using the same EC setup parameters. This variability is illustrated in a comparative table displaying the standard penetration depths of conventionally cast and rolled stainless steel (AISI 316 L SS) and PBF-LB manufactured 316 L SS at excitation frequencies ranging from 0.5 kHz to 100 kHz, as depicted in **Fig. 1**d.

2.2. Excitation frequency, f

The excitation frequency (Hz) refers to the frequency of the alternating current applied to the excitation coil to induce eddy currents in the material being tested. This frequency plays a crucial role in generating eddy currents and determines the depth of penetration of the eddy currents into the material, thereby influencing the sensitivity and resolution of the testing process. For example, a higher excitation frequency maximizes eddy current flow in the near-surface region and thus allows for the detection of small near-surface discontinuities [49]. Low-frequency tests are best suited for discontinuity inspection at greater



Frequency f [Hz]	Standard Penetration Depth δ [mm]	
	Cast 316L SS	PBF-LB 316L SS
500	19.36	16.03
1000	13.69	11.33
2000	9.68	8.01
3000	7.9	6.54
4000	6.84	5.67
5000	6.12	5.07
6000	5.59	4.63
7000	5.17	4.28
8000	4.84	4.01
9000	4.56	3.78
10,000	4.33	3.58
20,000	3.06	2.53
30,000	2.5	2.07
40,000	2.16	1.79
50,000	1.94	1.6
60,000	1.77	1.46
70,000	1.64	1.35
80,000	1.53	1.27
90,000	1.44	1.19
100,000	1.37	1.13

Fig. 1. Schematic representation of (a) eddy current (EC) flow in a specimen without and with a defect, (b) sectional views of internal defects of variable sizes within a Ti-6Al-4 V component processed by additive/subtractive hybrid manufacturing (ASHM) and the corresponding EC reactance signal perturbation due to defects (adapted from Du et al., [46]), (c) schematic illustration of the relationship between standard EC-penetration (skin) depth, δ and EC density, $\boldsymbol{J_e}$ (adapted from Spurek et al., [47]); and (d) comparative standard penetration depths of cast AISI 316 L SS and additively manufactured 316 L SS *via* powder bed fusion using a laser beam (PBF-LB) at excitation frequencies between 0.5 kHz to 100 kHz [48].

material depths, especially in ferromagnetic materials to compensate for their high magnetic permeability [42,50]. Therefore, adjusting the excitation frequency is essential to optimize the testing for different materials and applications, ensuring accurate and reliable results.

2.3. Magnetic permeability, μ

ECT is sensitive to the relative magnetic permeability, which is derived from the magnetic induction $\underline{B}$ in a material due to an external magnetic field $\underline{H}$. This relationship is expressed as follows:

$$\Delta B = \mu \Delta H \tag{3}$$

It is crucial to note that ECT assesses the relative magnetic permeability of the material (*i.e.*, a relative measure of a material's ability to be magnetized) rather than the actual magnetization state. Mathematically, relative magnetic permeability is given as $\mu_r = \mu/\mu_0$. During ECT, relative permeability is influenced by several factors, including heat-treatment, magnetization level, alloy composition, and residual stress, among others [51].

The different permeability states of different materials are described by a hysteresis curve shown in Fig. 2a. From Fig. 2a, we can understand that paramagnetic steels possess a relative permeability slightly greater than one, resulting in a flat hysteresis curve that transforms into a straight line characterized by low permeability (μ_r) and remanence (B_R). An example of a paramagnetic steel used in metal AM is 316 L austenitic stainless steel which has a relative permeability, μ_r, that ranges from 1.003 for 0 % cold work to 1.007 for 81 % cold work [52–54]. Conversely, magnetically soft steel displays a steep hysteresis curve featuring high permeability (μ_r) and remanence (B_R) but low coercivity (H_C,).

An example of this is the ferritic stainless steel class of materials used in metal AM is the hot rolled low carbon steel [DD11 (1.0332)] [55] with relative permeability between 500 and 2000 [56]. In the presence of an EC coil, the surface of paramagnetic steels such as 316 L SS experiences increased field strength, leading to higher eddy current density. This generates a larger secondary field that quickly diminishes the overall field strength just below the surface, resulting in reduced standard depth of penetration during ECT (refer to Fig. 2b and **Section 2.1**) compared to other less-permeable materials. Therefore, the higher relative magnetic permeability acts as a barrier, limiting the generation of eddy currents deeper within the part [51].

In general, an increase in conductivity or a decrease in permeability tends to decrease the measured impedance. Conversely, a decrease in conductivity or an increase in magnetic permeability typically leads to an increase in measured impedance. In practice, variations in magnetic permeability have a more significant impact on the effectiveness of ECT for crack detection than changes in material conductivity [57]. This is because magnetic permeability primarily influences eddy current flow, and its variations in ferrous materials can create “noise” that hinders the inspection of ferromagnetic materials like carbon steel welds [58]. Unlike conductivity, which affects penetration depth and current strength but is more predictable, permeability changes from non-flaw conditions mask discontinuities, limits penetration depth and reduces the ability to detect subsurface cracks [51].

2.4. Electrical conductivity, σ

Electrical conductivity measures a material's ability to conduct

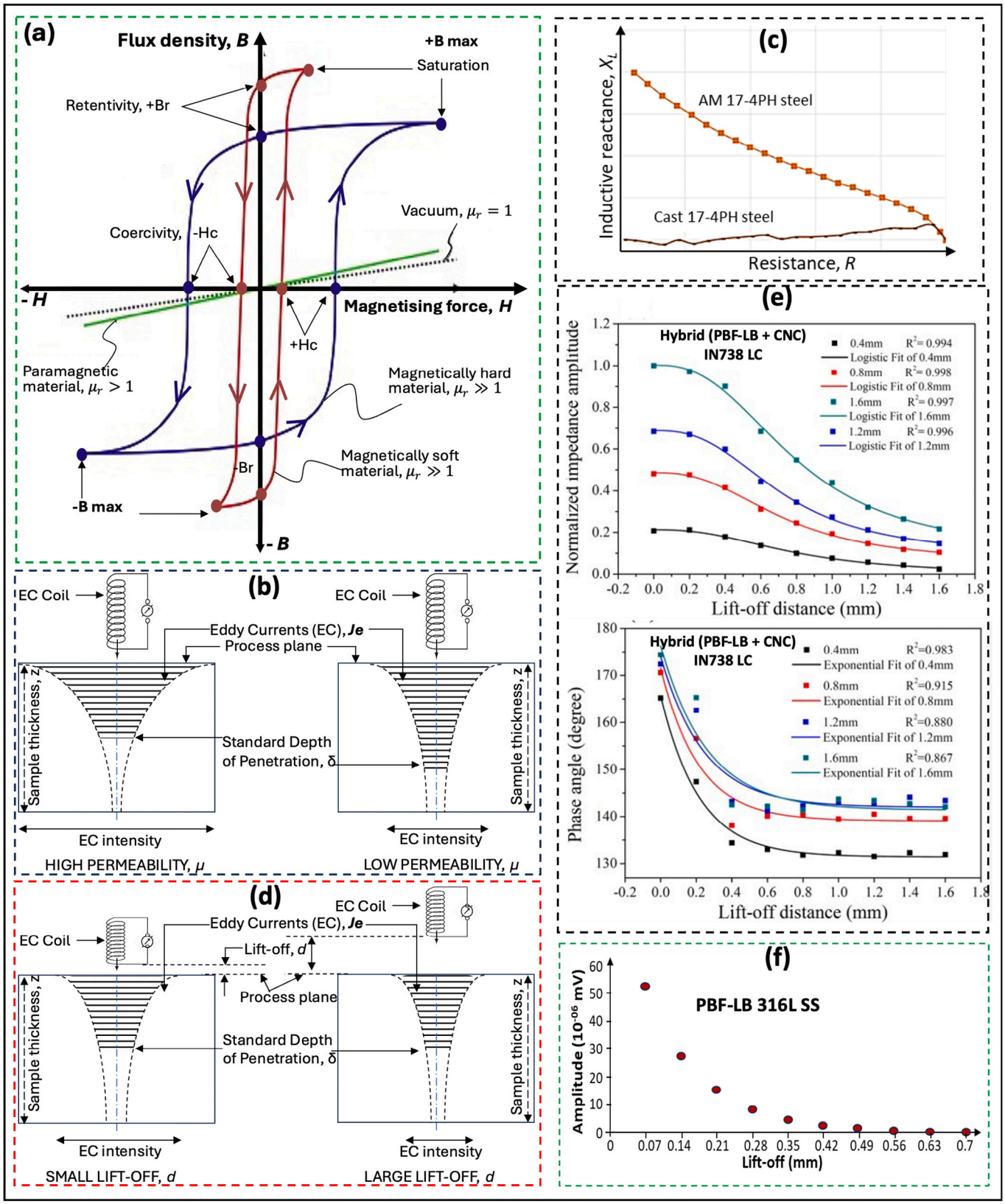


Fig. 2. (a) Superimposed representative hysteresis curves for magnetically hard, magnetically soft, and paramagnetic materials (© Authors); (b) schematic illustration of the effect of relative permeability on the magnitude and distribution of eddy currents (© Authors); (c) comparative of EC conductivity response a conventionally manufactured (cast) 17-4PH stainless steel standard conductivity specimen and a PBF-LB processed 17-4PH stainless steel specimen tested at an excitation frequency of 500 kHz (adapted from Schneider et al., [59]); (d)) schematic illustration of the effect of lift-off on the magnitude and distribution of eddy currents (© Authors); and the effect of lift-off distance on (e) the normalized impedance amplitude and impedance phase angle of defect EC signals in Inconel 738LC made by Additive/Subtractive Hybrid Manufacturing (PBF-LB + CNC) (adapted from Guo et al., [60]); and (f) the impedance amplitude of PBF-LB processed 316 L SS cylindrical component at an excitation frequency of 1 MHz (adapted from Saddoud [43]).

electricity and exists in both magnetic and non-magnetic materials. It is measured in % IACS (International Annealed Copper Standard), which describes how well currents flow through the tested material compared to copper using eq. (4). In materials of relatively high conductivity, strong EC is generated at the process plane (surface), which forms a strong opposing secondary electromagnetic field. As a result, the intensity of the EC field decreases rapidly with increasing depth below the surface. Conversely, in materials with lower conductivity, weaker eddy currents are generated near the surface, but they can penetrate to greater depths [51].

$$\sigma_{\%IACS} = \frac{172.41}{R\ (\mu\Omega/cm)} or \frac{\sigma_{S/m}}{5.8 \times 10^7 (S/m)} \times 100 = 172.41\ \sigma_{\mu S/cm} \tag{4}$$

where R is material resistance in $\mu\Omega/cm$ and $\sigma_{S/m}$ is material conductivity (S/m).

Both magnetic permeability and electric conductivity depend on the testing temperature, thickness (material volume), and microstructural state of the material (such as grain size and structure, work hardening, heat treatment, phases present from alloying and/or precipitates, etc). When the testing temperature increases, the material's conductivity also increases, resulting in a higher signal perturbation in the impedance plane [57]. This can potentially lead to a misinterpretation of defect signatures. The impedance plane, which will be explained further in **Section 2.6,** graphically represents the changes in the eddy current signal measurement response due to variations in material resistance. Therefore, a thicker material amplifies the effect of temperature on conductivity, although the rate of increase in conductivity diminishes as temperature continues to rise. The error in eddy current (EC) measurement induced by temperature can be estimated using eq. (5):

$$\sigma_T = \sigma_{T_0} \times [1 + \alpha \Delta T] \tag{5}$$

where σ_T and σ_{T_0} represent the corrected electrical conductivity at temperature T and the electrical conductivity at reference temperature T_0, respectively. The thermal expansion coefficient of the alloy, and the temperature difference $\Delta T = T - T_0$, are denoted as α and ΔT respectively.

The apparent electrical conductivity of the samples at room temperature ECT may be used to characterize the density of the component as will be discussed in **Sections 3** and **4**. However, the tendency of electric current concentration near the surface of the process plane poses a negative effect on the depth of penetration of the EC density. This affects the detection of deep flaws such as pores/porosities within the tested sample due to the skin effect phenomena described in **Section 2.1** [43]. According to ASTM E1004—21 [18], the sample thickness for electrical conductivity measurement should be at least 2.6 times the standard depth of penetration (δ) of the induced EC's, as calculated. Moreover, the sample manufacturing technique also affects the electrical conductivity of the samples during EC testing as shown in Fig. 2c [59]. More about this will be discussed in **Section 0.**

2.5. Lift-off, d

ECT is sensitive to the distance between the probe and the material being inspected, known as lift-off, d (mm). As lift-off increases, the interaction between the probe's coil and the material weakens (refer to Fig. 2d). This reduces the amplitude and phase angle of the eddy currents generated, making it difficult to distinguish flaws from normal variations in the material [43,48]. The consequence of a very large lift-off is that EC field intensity at the surface becomes narrow (refer to Fig. 2d), and no signal may be detectable. While achieving a zero lift-off, d_0 is not always necessary, however maintaining a consistent distance and compensating where necessary, is crucial.

The study by Lim et al., [61] specifically addresses the impact of varying lift-off distances during electrical conductivity measurements of PBF-LB processed Ti-6Al-4 V specimens, using ECT. They compensated for this effect by estimating the zero-lift-off phase value, $\varnothing_{d0}$ using a modified theoretical approach derived from phase value and lift-off distance measurements. The developed theoretical model mathematically described in eq. (5) shows that the phase angle variation with lift-off distance follows a simple exponential function.

$$\varnothing_{d0} = \varnothing_d - \beta d e^{-2\alpha d} \tag{6}$$

where $\varnothing_d$ is the eddy-current phase value at an arbitrary lift-off distance (d), α and β are calibration coefficients described in [61]. Therefore, the phase value at any arbitrary lift-off distance can be normalized to the zero-lift-off phase value using eq. (5).

The study by Guo et al., [60] suggests that the relationship between lift-off and impedance amplitude is logistic (*i.e.*, it tends to follow an S-shaped curve), but with phase angle, the relationship is exponential as shown in Fig. 2e for additively manufactured Inconel 738LC. This shows that the phase angle is more sensitive to changes in lift-off compared to the amplitude. However, Saddoud [43] reported that the effect of lift-off on the impedance (signal) amplitude is exponential for PBF-LB processed 316 L SS at a single excitation frequency of 1 MHz, as shown in Fig. 2f. While these are the only studies identified in the literature by the authors of this review article, the differing findings suggest that the lift-off response is highly dependent on the specific metal AM alloy, highlighting the necessity of optimizing lift-off parameters for each material tested.

2.6. Impedance plane, Z

Electrical impedance, measured in ohms (Ω), signifies the overall resistance a circuit opposes to an alternating current. During ECT, Z is primarily affected by material resistance, R, and inductive reactance X_L. An impedance plane is a graphical representation of the complex probe impedance in ECT and is mathematically simplified in eq. (6).

Fig. 3 presents the complex eddy current impedance plane. It typically features resistance plotted on the x-axis (horizontal), inductive reactance on the y-axis (vertical), and integrates all the ECT factors previously discussed. The variations in the strength of eddy currents and the magnetic permeability of the test material influence the eddy current signal, allowing for the characterization of material defects like cracks, and estimation of physical properties such as electrical conductivity [62]. Although the general form of the impedance plane remains consistent, the specific characteristics vary depending on the EC-probe type and frequency used.

$$Z = R + jX_L = \sqrt{R^2 + X_L^2} \tag{7}$$

where Z represents the complex impedance and j is the imaginary unit for which $j\ 2 = -1$. The inductive reactance $X_L = 2\pi fL$, is directly proportional to the excitation frequency (f) and the induction coefficient (L) when a test piece is in proximity to the coil during ECT. In the impedance plane, changes in the location of the material point are a function of $\sqrt{a w \sigma \mu}$, where a represents the coil radius, and ω is the angular frequency [63]. Impedance is also related to the phase angle, ∅ of the circuit by the following equation:

$$tan\varnothing = \frac{X_L}{R} \tag{8}$$

2.7. Probe configuration

The choice of eddy current probe (EC-Probe) significantly influences the desired detection sensitivity and suitability for specific materials or applications. Based on the design and operational modes, traditional ECT probes are generally of absolute, differential, and reflection types [64–66]. A selection of examples of conventionally manufactured and where available, additively manufactured components are discussed below hereafter. Specific AM case studies are presented in **Section 3.**

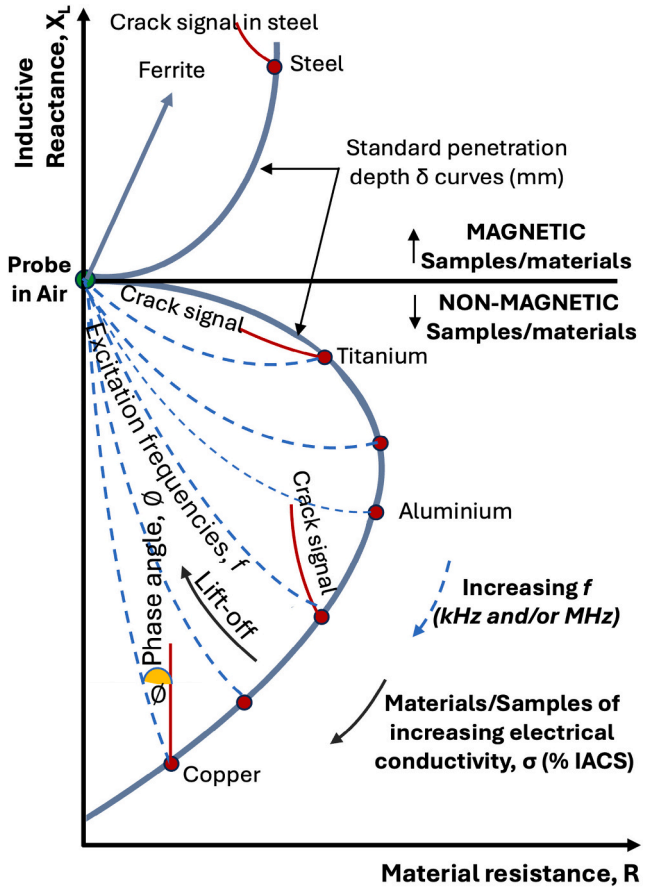


Fig. 3. Schematic illustrations of complex eddy current impedance plane (© by Authors).

2.7.1. *Absolute probes*

The absolute EC-probes feature a single test coil responsible for both generating eddy currents in the material and detecting changes in these currents as shown in Fig. 4a. Absolute EC-probes measure the absolute change in impedance of the test coil, offering initial insights into the characteristics of the test material. It is by far, the most used EC probe in metal AM testing.

However, absolute probes are sensitive to factors such as conductivity, permeability, lift-off, temperature, and material/sample thickness (due to limited standard penetration depths) [43,60]. Therefore, when these variables are pertinent to the inspection being conducted, differential or reflection EC-probes are often used instead.

2.7.2. *Differential probes*

Differential EC-probes typically feature two active coils wound in opposition, as shown in Fig. 4a. When both coils are positioned over a defect-free area of the test sample, no differential signal is generated because they are both examining the same material. However, if one coil is positioned over a defect while the other is over the defect-free region of the material, a differential signal is produced. Differential probes excel in detecting defects with high sensitivity while being relatively insensitive to gradual changes in properties, such as conductivity, permeability, and probe movement compared to absolute EC probes.

Nevertheless, interpreting the signals may pose challenges, especially if a flaw extends beyond the spacing between the two coils. Therefore, they are best suited for detecting small near-surface defects and the evaluation of material thickness. The article by Bell & Birks [64] provides an extended list of other pros and cons between absolute and differential EC probes.

2.7.3. *Reflection probes*

In contrast to differential EC-probes, reflection EC-probes operate based on the principle of electromagnetic wave reflection. Reflection EC-probes typically consist of two coils, resembling the setup of a differential probe. However, in this configuration, one coil is dedicated to inducing eddy currents within the test material, while the other coil detects changes in the material. These types of probes are commonly known as driver/pickup probes. One of the key advantages of reflection probes is their ability to separately optimize the driver and pickup coils for specific functions. This means that the driver coil can be designed to generate a robust and uniform magnetic field near the pickup coil, while the pickup coil can be engineered to be highly sensitive, allowing it to detect even the smallest defects. Reflection probes are commonly used for detecting and characterizing subsurface defects, such as cracks, voids, or inclusions, in metallic and non-metallic materials.

To summarise, absolute probes measure the absolute change in impedance of the test coil, while differential probes measure the difference in impedance between two coils, and reflection probes use electromagnetic wave reflection to sense the changes in the test material. Each type of probe has its advantages and limitations, and the choice of probe depends on the specific inspection application.

2.7.4. *Magnetoresistive (MR) probes*

Magnetoresistive (MR) EC probes differ significantly from traditional absolute, differential, and reflection EC-probe types (**Sections 2.7.1–2.7.3**). MR EC-probes operate on the principle of the magnetoresistive effect, measuring changes in electrical resistance due to a magnetic field. In contrast, traditional EC-probes rely on electromagnetic induction, detecting impedance changes caused by an applied electrical current. Furthermore, while traditional EC-probes utilize pickup coils, MR EC-probes employ magnetoresistive sensors made of materials like composite semiconductors such as InSb or Permalloy [68] or an oxide layer, in single or multi-layer (stacked) film or pad configurations. The resistance change in these sensor materials is typically proportional to the strength of the applied magnetic field and is independent of the field's orientation [68].

MR EC-probes combine traditional EC principles with the unique properties of magnetoresistive materials. Consider two MR EC-probes with uniform properties (*e.g.*, MR1 and MR2) to be connected in series, a magnet will impose a uniform magnetic field on both MR probe's (Fig. 4b-1). An output terminal is positioned at the connection point between the two MR probes, and the voltage at this terminal is referred to as the output voltage. When a voltage, V is applied across the terminals of the MR devices, the output voltage is approximately half of V, termed the median voltage (stage 1 in Fig. 4b-2). However, if the magnetic fields acting on MR1 and MR2 differ, the output voltage deviates from the median due to differing resistance values in the probes. If a strong magnetic field is applied to MR1, its resistance increases more than MR2, resulting in an output voltage lower than the median. Conversely, if a strong magnetic field is applied to MR2, the output voltage increases by $1/2V$.

This principle also applies when detecting magnetic materials. If a magnetic material, such as a piece of iron or steel component, approaches one of the MR EC-probes (*e.g.*, MR2), the magnetic field near the material becomes polarized. As a result, MR2 experiences a stronger magnetic field compared to MR1, increasing its resistance and causing the output voltage to rise (see stages 2 and 3 of Fig. 4b-2). This is illustrated in Fig. 4b-3, which shows the positional relationship of the response output voltages of two MR sensors (MR1 and MR2) in proximity to a magnetic test material. MR-based EC techniques are discussed in **Section 2.9**, and more details on the general principles and methodologies of MR probes can be found in the studies of Elzwawy et al. [70] and Rifai et al., [71].

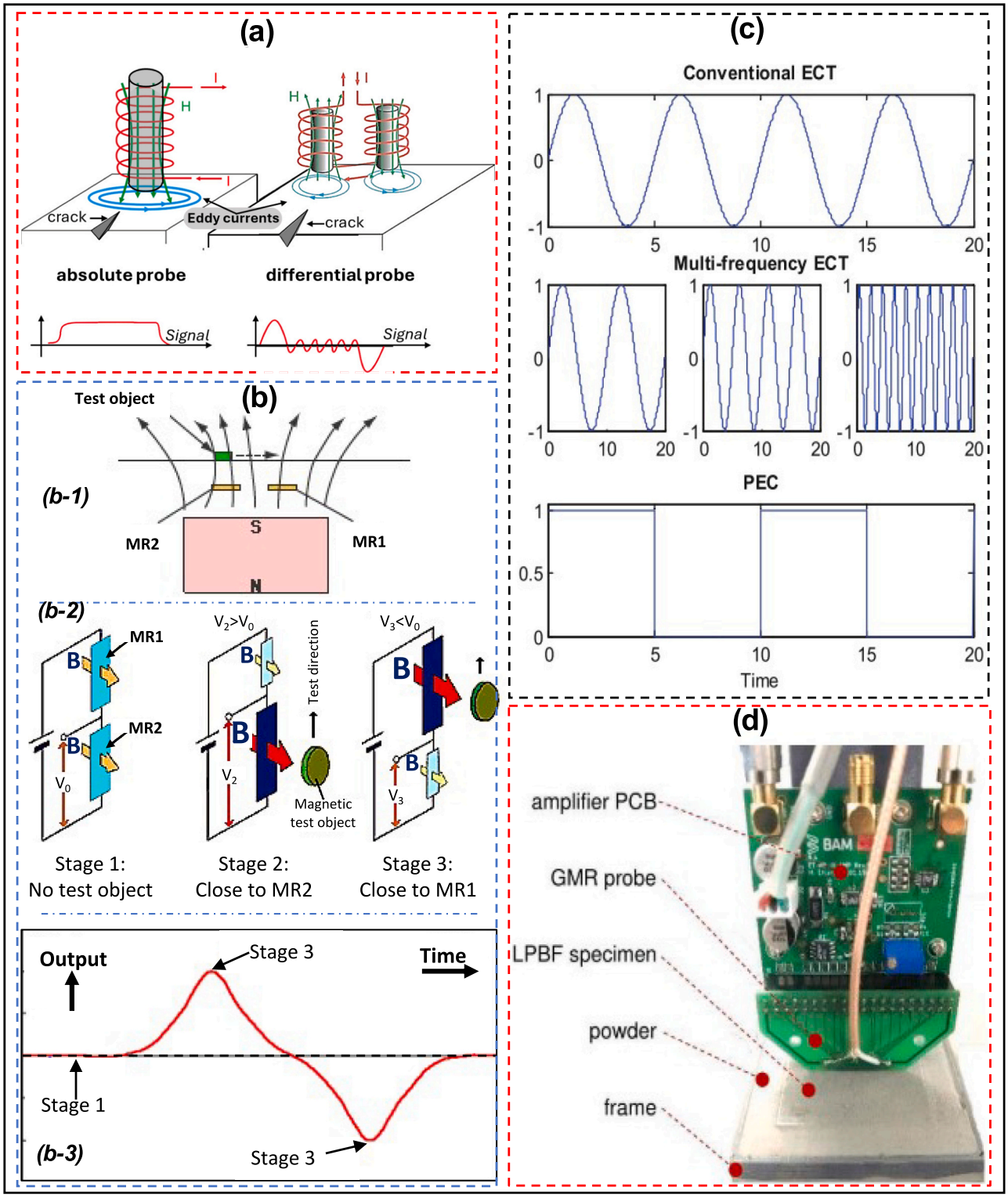


Fig. 4. Schematic illustrations of (a) absolute and differential eddy current probe types, with corresponding typical signal output in response to a crack in a test object (adapted from [42,67]); (b) excitation waveform of single-frequency eddy current technique (ECT), multi-frequency ECT, and Pulsed-ECT [50]; (c) schematic illustrations of a test object in the magnetic field of two magnetoresistive (MR1 and MR2) sensors in C-1; C-2 and C-3 illustrate the changes in output voltage (V_0, V_2 and V_3) and flux density, *B* as a magnetic material moves past the front surface of the two MR sensors (adapted from [68], and (d) picture of a giant magnetoresistive (GMR) probe [69].

2.8. ECT techniques based on their excitation signals

There are various reviews [42,50,57,71–77] on ECT techniques for various quality control applications and material testing. From these reviews, particularly the reviews by AbdAlla et al. and Sophian et al. [57,73], the authors of this article have identified several ECT methods that demonstrate versatility in conventional material testing and potential relevance to metal AM. The identified ECT techniques include the

Single-frequency eddy current (SFEC) and isotropic ECT technique, the Multi-frequency eddy current (MFEC) technique, and the Pulsed eddy current (PEC) technique. These techniques are categorized primarily based on their excitation signals. Each of these ECT's will be briefly described below, along with relevant case studies where applicable.

2.8.1. Single-frequency eddy current (SFEC) and isotropic ECT technique

The single-frequency eddy current (SFEC) and isotropic ECT techniques are widely employed for surface and near-surface crack detection. It utilizes an alternating current of a single frequency, or more precisely, over a very narrow frequency bandwidth [78], to induce sinusoidal eddy currents in the material, as shown in Fig. 4c. Note that SFEC is different from isotropic eddy current (ISEC) testing which uses a larger broadband of frequencies. Compared to ISEC, the SFEC technique has limitations in penetration depth and spatial resolution for defect detection, higher lift-off sensitivity, limited material characterization (not suitable for assessing hardness, grain structure, electrical conductivity, and magnetic permeability), limited adaptability to material changes, and limited capability for testing high-conductivity materials. For example, to examine deeper sub-surface defects such as porosities and lack-of-fusion which can in PBF-LB/EB processed components, the excitation current can be increased, but this results in probe heating which could alter the measured signal. Alternatively, lowering the frequency reduces sensitivity due to the skin effect [79] as discussed in **Section 2.1**. These limitations are addressed by using alternative techniques such as multi-frequency eddy current and pulsed eddy current techniques, which have several advantages over conventional SFEC techniques.

2.8.2. Multi-frequency eddy current (MFEC) technique

In MFEC testing, multiple discrete excitation frequencies (refer to Fig. 4c) are applied sequentially to analyze microstructure and defects in greater detail, particularly those with complex shapes. This approach allows for the identification of flaws amidst variations in conductivity, permeability, geometry, and probe lift-off, by subtracting the confounding characteristic signals arising from these variations [80]. Lu et al., [81] proposed an inverse method to subtract these confounding cross-sensitivities to the characteristic signals of these variations. They successfully reconstructed the arbitrary permeability and evaluated the effect of conductivities, sample thickness, and lift-off during MFEC testing of dual-phase steel samples (DP600, DP800, and DP1000).

Given these advantages of MFEC over SFEC testing, Belkacem et al., [80] successfully demonstrated the MFEC's capability to accurately measure the sheet resistance of a complicated-to-measure epitaxy-grown GaN-doped sample. Similarly, Zhou et al., [82] used MFEC for studying the microstructures in bias weld of coiled tubing steel strip, while Bobrov & Epp [83] utilized MFEC to examine the heat treatment conditions of steel 100Cr6 (AISI 52100) in various states, including spheroidized carbide, bainitic, martensitic quenched, and tempered states. These studies indicate the applicability of MFEC in measuring melt layer thickness, and for tracking the microstructural evolution of the as-built component during PBF-LB and PBF-EB processes. So far, only one study by Obaton et al., [84] utilized the MFEC for *ex-situ* density evaluation of PBF-LB processed components, details of which will be discussed in **Section 3.**

It is important to note that the MFEC technique is often confused with the sweep (or swept)-frequency eddy current (Swept-FEC) technique. However, both techniques differ and serve distinct purposes. Specifically, MFEC operates with a limited number of discrete frequencies in one test pass, whereas Swept-FEC employs a continuous wide range of frequencies in one test pass [49]. Therefore, Swept-FEC requires specialized equipment for optimal performance [85,86]. Swept-FEC is particularly well-suited for depth information measurement tasks like the thickness of coatings and the estimation of crack location on the inner skin, a second layer, or an outside skin of a test component [86]. While Swept-FEC can be performed using commercial EC equipment, the process is complex, time-intensive, and has not yet been explored for metal AM testing. For this reason, Swept-FEC will not be discussed further in this review due to the lack of supporting literature.

2.8.3. Pulsed eddy current (PEC) technique

Pulsed eddy current (PEC) techniques utilize pulse waveforms as shown in Fig. 4c to excite induction coils across a wide-band frequency spectrum, unlike conventional sinusoidal ECT techniques such as SFEC. Larger excitation coils may be necessary at lower excitation frequencies. PEC response data can be analyzed in either the time domain, frequency domain, or both. While PEC operates at multiple frequencies simultaneously and provides the opportunity to simultaneously analyze responses across a wide frequency range, the MFEC techniques apply different excitation frequencies sequentially. Thus, PEC offers a broader frequency range and increased penetration depth compared to MFEC. Additionally, PEC provides advantages over single-frequency methods, including reliable operation at significant lift-off distances (up to 100 mm), increased penetration depth, simultaneous operation at multiple frequencies, and enhanced defect information during complicated material testing like corrosion, plastic deformation, and fatigue [50].

For instance, Zhao et al. [87] utilized the PEC technique to effectively differentiate corrosion defects within metal pipelines from those on the exteriors. Fang et al., [88] introduced a PEC signal processing approach based on empirical modal decomposition (EMD) to discern between plastic deformation and fatigue damage. Their analysis of PEC signal characteristics led to the development of an assessment method for distinguishing fatigue damage with preset plastic deformation in 304 SS nuclear components. This study by Fang et al., [88] is more pertinent to metal AM component assessment *via* ECT, given the layer-wise build strategy and inherent surface roughness, porosities, and narrow cracks that affect the fatigue life of AM components negatively, during service. For a more comprehensive understanding of the PEC technique, readers are encouraged to consult Refs [50, 72, 89].

2.9. Magnetoresistive (MR) sensor-based ECT techniques

Traditional induction coils, as used in excitation signal-based ECT techniques discussed in **Section 2.8**, are not necessarily bulky. However, they have limited detection capabilities, particularly for small cracks, due to their insensitivity to gradual magnetic field changes [50]. In contrast, magnetic field transducers such as magnetoresistive (MR) sensors (see **Section 2.7.4**) and Hall effect devices operate independently of excitation signals. These transducers provide several advantages, including superior defect sensitivity (enhanced spatial resolution), the potential for miniaturization, higher frequency bandwidths, and simultaneous testing of larger process plane areas depending on the array length [90]. The two primary MR-based ECT techniques are Giant Magnetoresistance (GMR) and Tunnel Magnetoresistance (TMR) ECT techniques often fabricated in arrays, but differ in their underlying mechanisms, structure, and performance characteristics. An exemplary picture of a GMR is shown in Fig. 4d.

2.9.1. Tunnel Magnetoresistance (TMR) ECT technique

The structure of Tunnel Magnetoresistance (TMR) sensors is composed of two or more ferromagnetic layers separated by thin insulating barriers (typically a few nanometres thick), resulting in a magnetic tunnel junction [91]. A simplified Magnetic tunnel (MT) junction structure is FM1/I/FM2, where FM is a ferromagnetic layer and I is an insulating layer. The underlying detection mechanism is such that electrons tunnel through the insulating barrier during which the resistance of the junction changes depending on the relative orientation of the magnetic spins in the ferromagnetic layers. The tunneling process is a quantum mechanical phenomenon, given that traditional physics forbids a true physical tunneling process [91]. The direction of the magnetizations of the ferromagnetic layers changes with the external

magnetic field. If the magnetizations are aligned in parallel, the electrons are more likely to tunnel through the insulating layer resulting in a lower resistance in the output signal, than if they are aligned in opposite (anti-parallel) directions (*i.e.*, lower tunneling probability and higher resistance). This resistance change is influenced by the spin polarization of the ferromagnetic layers and the tunnelling effect. In a multi-stack TMR, the rate of change of the resistance is represented by the MR ratio, which often exceeds 100 % in MgO-based MT junctions.

TMR sensors offer several advantages, including high sensitivity, an extended operating frequency range (from DC to several MHz), and excellent temperature stability compared to excitation signal-based ECT techniques. For instance, Pelkner et al. [92] demonstrated the superior performance of an ECT array probe comprising 32 TMR elements over conventional absolute and differential EC-probes, for detecting small adjacent boreholes and micro-notches in aluminium and titanium plates. The conventional EC probes operated at a current, I, and excitation frequency, f of 200 mA and 310 kHz, respectively. The TMR array was operated at f = 1.3 MHz and I = 100 mA. The boreholes in the aluminium plate had a diameter of 0.44 mm and a depth of 0.25 mm, with a center-to-center separation ranging from 0.6 mm to 2 mm (see **Fig. 5**a). Using the TMR array probe, the researchers achieved high spatial resolution due to the compact size of the TMR sensor elements, which have a length of approximately 60 µm, enabling near "point-like" measurements. The TMR probe demonstrated a good signal-to-noise ratio (SNR) and was able to resolve and distinguish neighbouring boreholes, outperforming the tested conventional eddy current probe. In contrast, both the absolute and differential EC-probes failed to reliably separate the adjacent boreholes as shown in **Fig. 5**b - e.

In another study, Caetano et al., [93] proposed two magnetoresistive (MR) sensor-based probes optimized for high sensitivity and spatial resolution. One probe had 8 TMR's and the other with 32 TMR's. A custom application-specific integrated circuit (ASIC) was developed and used for signal processing and interfacing. The TMR's were able to detect defects with diameters as small as 0.44 mm, and pitches of 0.6 mm, at edge distances ≥0.16 mm.

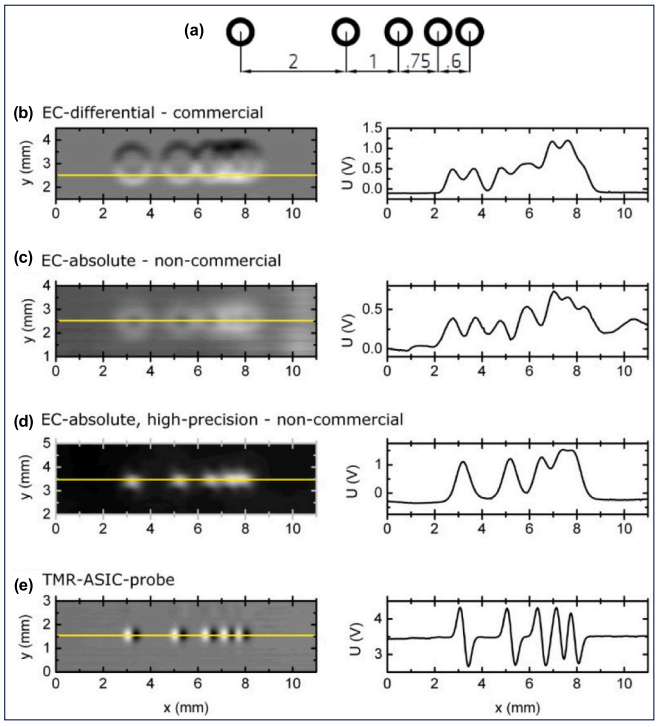


Fig. 5. (a) Schematic representation of bored holes in an aluminium sample, spaced at distances of 0.6 mm, 0.75 mm, 1 mm, and 2 mm. Gray-scaled EC plots (left) and corresponding defect signals (right) are shown for various probes: (b) differential probe, (c) absolute probe, (d) absolute high-precision probe, and (e) TMR-ASIC probe. Adapted from Pelkner et al. [92]. The results highlight the superior detection sensitivity and performance of TMR-based ECT techniques.

2.9.2. *Giant magnetoresistance (GMR) ECT technique*

Similar to TMR's, GMR sensors are solid-state magnetic sensors that can be arranged in compact arrays on circuit boards with spacing as small as 5 µm [94]. It's structure consists of two or more ferromagnetic layers separated by non-magnetic layers. The resulting simplified structure is FM1/NM/FM2, where FM is a ferromagnetic layer and NM is a non-magnetic layer. Compared to the MR ratio of TMR's, GMR exhibits a much lower MR ratio of about ~10–20 % for most applications [91]. This makes GMR's more susceptible to noise and temperature variations than TMR's. Compared to excitation signal-based ECT's, GMR's offer higher sensitivity and lower power consumption, with the added advantage of having a less complex and cheaper manufacturing process compared to TMR's. This later reason partly explains why ECT on metal components using GMR's and GMR optimization studies are more readily available in literature than for TMR's.

Berkache et al., [95,96] evaluated the performance of two different EC sensors to detect short thin external cracks in AISI 304 austenitic and SA106 carbon steel pipe girth welds in offshore structures. The authors showed that the conventional sensors with air coils arranged parallel to the test surface have the highest SNR to detect narrow and small artificial cracks. The best EC setup had a length of 19.2 mm (effective scanning area) comprising 32 GMR elements arrayed at 0.6 mm intervals. The GMR-based ECT sensors were oriented at 45 ^{o} to the array length, to prevent their saturation by the magnetic field of the exciting coil. The authors further demonstrated the effectiveness of their approach by finite element simulation and experimentally validating the technique on an aluminium block with different surface defects.

Bui et al., [97] recently developed a high-resolution flaw mapping system using an 8-element GMR EC probe array with a spacing of 5.6 mm. The system was tested on two samples: Sample A, featuring six artificial notches (7 mm in length and 0.6 mm in width) on an aluminium surface, and Sample B, containing thermal fatigue defects (see Fig. 6a-1 and **a-2**). The experiments were conducted with an excitation current of 50 mA and optimal excitation frequencies of 70 kHz for Sample A and 95 kHz for Sample B. At these excitation frequencies and current, the SNR was 60.7 dB and 59.8 dB, respectively. The system demonstrated its ability to detect multi-orientation cracks and thermal fatigue defects in an aluminium component (see Fig. 6a-3 and **a-4)**, with experimental verification of its performance. Notably, they achieved a crack separation resolution of <2 mm directly from the raw GMR EC scan data, removing the need for post-image processing to extract features. In addition to the superior detection capability and sensitivity of the GMR probe, the researchers reported a significant reduction in overall inspection time—more than fivefold—compared to using a single GMR EC probe, which is also typical of traditional single-probe ECTs discussed in **Section 2.8**. A similar study on artificial notches on Aluminium plates was carried out by Nyuyen et al., [98], for which the researchers also reported excellent detection capability and sensitivity of GMR with distinct response signals as shown in Fig. 6b-1 **to b3.**

Other EC-studies using GMR include the works by Bailey et al., [99] for corrosion detection in an insulated metal pipe, design optimization of GMR's by Romero-Arismendi et al., [100], and in embedded flaw detection in 304 L stainless steel sample by Vacher et al., [101].

The selected EC studies on conventionally manufactured components highlight that MR-based ECT provides superior sensitivity, portability, array configurability, flexibility, higher spatial resolution, and enhanced defect detection capabilities, which can be further augmented with advanced signal processing techniques. These advantages make MR-based ECT a promising technology for both *in-situ* and *ex-situ* EC testing of AM components. While no studies on the application or adaptation of TMR-EC testing for AM components were found in the literature, an exemplar study on the use of GMR for EC testing of AM

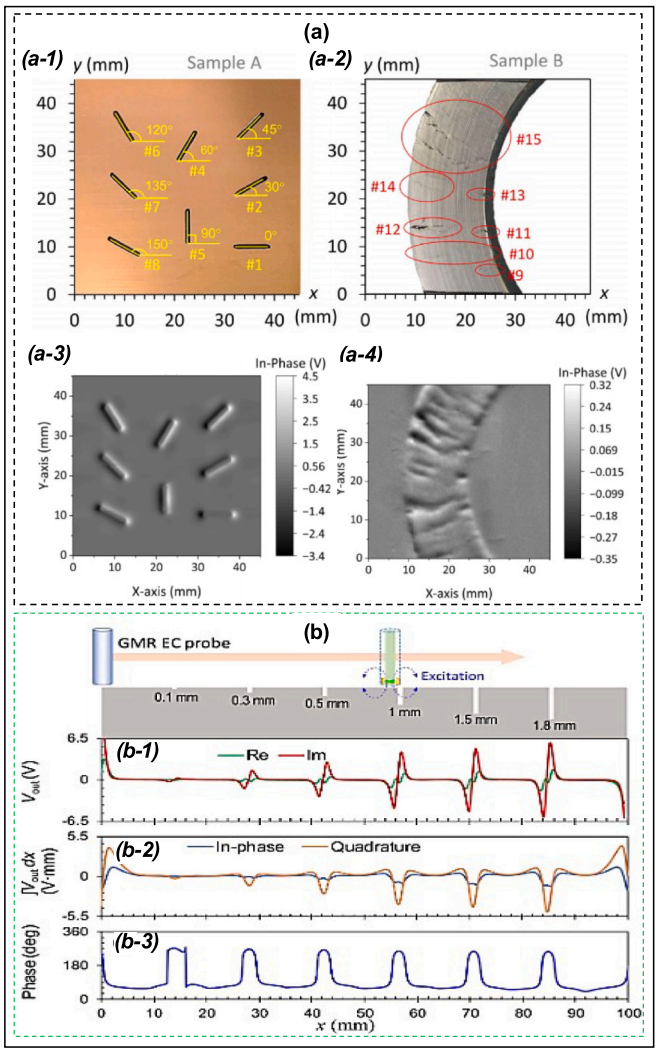


Fig. 6. (a) Schematic representation of notches in aluminium sample A alongside an image of thermal fatigue cracks in aluminium sample B (*a-1* and *a-2*); (*a-3*) Gray-scaled in-phase GMR-EC plots of artificial notches in sample A scanned along the x-direction at an excitation frequency of 70 kHz; and (*a-4*) Gray-scaled in-phase GMR-EC plots of thermal fatigue defects in sample B scanned along the x-direction at an excitation frequency of 95 kHz (adapted from Bui et al., [97]); (b) Output GMR signals of notches on an aluminium plate at the excitation frequency of 35 kHz; (*b-1*) In-phase real (Re) and quadrature or imaginary (Im) response signals; (*b-2*) Integrated in-phase (Re) and quadrature (Im) signals; and (*b-3*) integrated phase signals (adapted from Nyuyen et al., [98]).

components is discussed in **Section 3.4.**

Another ECT technique, that is not highly relevant or applied in assessing metal AM components, is the Remote Field Eddy Current (RFEC) technique [102–104]. This technique is best suited for detecting defects in ferromagnetic cylinders and tubing. Additionally, the Superconducting Quantum Interference Devices (SQUID)-based EC technique, which requires cryogenic cooling to typically below 10 K and has high operational costs, is also not directly applicable to AM component assessment [105,106].

3. *Ex-situ* eddy current testing on metal AM components

Expanding upon the foundational principles and practical applications of ECT outlined in **Section 2**, this section focuses exclusively on the limited available studies demonstrating ECT's potential for *ex-situ* inspections of metal AM components. A comprehensive summary of these *ex-situ* studies is provided in Table 1.

3.1. *Ex-situ* ECT for defect detection and density estimation

Engineered surface defects in PBF-LB processed 316 L SS [43], artificial sub-surface defects (*e.g.*, notches and holes) in PBF-LB processed Ti-6Al-4 V [66], 316 L SS [66,107], and Co-based alloy samples processed *via* PBF-LB and PBF-EB [108] have been investigated. More so, the detection of the keyhole porosity and lack of fusion defects in PBF-LB processed 316 L SS coupons [109], has also been demonstrated. Hippert et al. [110] also investigated the effectiveness of ECT to inspect the delamination of PBF-LB processed 316 L SS, due to thermal stresses.

Ex-situ ECT has also been implemented in components made by additive/subtractive hybrid manufacturing (ASHM), a process that combines either DED or PBF-LB with CNC milling. An example of this is the study by Du et al. [46], implementing *ex-situ* ECT to investigate engineered sub-surface defects in the ASHM-processed Ti-6Al-4 V component. The specific AM technique employed in their work was DED. A similar *ex-situ* ECT study by Guo, et al. [60] was performed on an ASHM-processed Inconel 738LC test coupon, where PBF-LB was the AM technique employed.

Across these studies, micro-computed tomography (μCT) has been consistently employed to measure the volume and precise dimensions of artificial defects or engineered porosity deliberately introduced through selective process parameter adjustments in PBF-LB. This process often involves customized signal processing methods, such as detection algorithms, to segment EC data into layers and spatially align it with μCT data. The resulting alignment enables visual validation of the EC impedance amplitude signals through 2D contour plots, as shown in Fig. 7a.

The aforementioned studies achieved indirect characterization of engineered/artificial defects by comparing detected defects from ECT against known defect dimensions and geometries, rather than directly from the ECT data itself. However, successful demonstrations of direct ECT evaluations have been reported for Ti6Al4V lattice structures [84], AlSi10Mg [111,112], and 316 L SS dense (solid/bulk) components [111,113]. These direct estimations leverage differences in detected electrical conductivities, which correlate with material densities (*i.e.*, relative densities). These estimations are typically cross-validated with relative density data obtained through the Archimedes method. Refer to Table 1 for the ECT parameters adopted.

An example of a 2D ECT contour image representing EC-measured electrical conductivity is provided in Fig. 7b, depicting ten PBF-LB processed 316 L SS test samples with different relative densities [111]. A linear correlation between relative density and EC-measured electrical conductivity was also reported in both studies by Refs. [111, 113], who examined PBF-LB processed dense 316 L SS and AiSi10Mg samples, as illustrated in Fig. 7c. Additionally, Obaton, et al., [84], demonstrated ECT's capability to distinguish Ti6Al4V lattice structures with varying cell percentages by analyzing differences in the slope of quasi-linear curves of EC-measured electrical conductivity (Fig. 7d). Moreover, Spurek et al., [111] showed that ECT could statistically detect minute relative density differences as small as 0.05 % in PBF-LB processed 316 L and AlSi10Mg cubic samples.

3.2. *Ex-situ* ECT for the electrical conductivity estimation

In a study by Gruber et al., [114], they examined various wall thicknesses using the eddy-current method to understand how sample thickness and inherent surface quality affect the measured electrical conductivity of PBF-LB processed pure copper samples. The ECT parameters are summarised in Table 1.

The study found that surface roughness had a detrimental effect on the estimated electrical conductivity of the copper samples. This effect is illustrated in Fig. 8a, where electrical conductivities were notably improved when the copper sample surfaces were milled. Additionally,

Table 1
Overview of *ex-situ* eddy current testing of metal AM components.

Reference	Focus	AM type(s)	Material(s)	Defect type(s)	Sensor type/method(s)	Optimal/tested parameter(s)	Finding(s)
Saddoud et al., [43]	Artificial defect identification	PBF-LB	316 L SS	12 *Notches* (1–40 mm L x 0.3 mm W x 0.1–0.5 mm depth). 9 *Holes* (0.15–0.5 mm diameter × 0.1–0.5 mm depth	**1).** Separate transmitter/receiver sensor **2).** Isotropic sensor	f = 1 MHz, Voltage = 5 V, Step size = 0.1 mm, Scan speed = 5 mm/s	The isotropic sensor is most effective for detecting and characterizing defects with unknown orientations.
Du, W, et al. [46]	Effect of excitation frequency, residual heat, and lift-off distance on ECT.	Hybrid (DED + CNC)	Ti-6Al-4 V	Sub-surface rod-like defects of 0.2–0.8 mm widths.	Absolute EC probe in impedance sweep mode	f = 100 kHz, d = 0.2 mm, voltage = 2.0 V, gain = 50 dB, and scan speed = 500 mm/min).	**1).** An increase in sample surface temperature resulted in a quasi-linear increase in the normalized magnitude of inductive reactance. **2).** As the lift-off distance increased from 0.08 to 1.4 mm, the normalized magnitude of both inductive reactance and resistance decreased for each frequency investigated. **3).** Detection depth of 1.2 mm and successful identification of defects with a size of ≥0.2 mm were achieved.
Geľatko et al., [48]	Artificial defect identification	PBF-LB	316 L SS	Internal rectangular cavities (L = 10 mm, W = 5 mm, and 2 mm depth) Grooves of 0.2 mm in width and depths of 0.2–5 mm. Blind holes of 0.10 to 2.50 mm radii and depth of 2 mm.	Portable NORTEC 600 with 3 absolutes (single coil) probes.	f = 5 to 90 kHz, Hgain = 42.4 to 71 dB, Vgain = 90 to 225 dB, Φ = 40 to 225 °	**1).** SWEEP mode is best for inner defects in the subsurface layer **2).** IMPEDANCE mode is better for surface-reaching defects. **3).** The smallest defect detected was 0.5 mm in diameter. **4).** Maximum detection depth was 6.5 mm.
Guo et al., [60]	Effect of excitation frequency, defect depth and size, lift-off distance, surface roughness, and residual heat on ECT.	Hybrid (PBF-LB + CNC)	Inconel 738LC	Four (4) sub-surface cylindrical defects of 0.4–1.6 mm diameter.	Differential EC probe with a core diameter of 5 mm.	f = 30 to 1000 kHz, d = 0.07 to 1.60 mm, gain = 35 dB, and scan speed = 600 mm/min	**1).** Optimal f = 170 kHz **2).** Exponential relationship between lift-off and EC signals. **3).** ECT is capable of detecting defects at sample surface temperatures up to 300 °C. **4).** Surface roughness compromises signal amplitude but does not influence the phase angle of defect EC signals.
Obaton et al., [84]	Density evaluation	PBF-LB	TiAl6V	30 cubic lattices with different lattice dimensions	Multi-frequency ECT with 12 mm-diameter transducers (Sciensoria *Z*-Scope*7)	f = 1 MHz	**1).** Negligible effect of surface roughness. **2).** Quasi-linear relationship between electrical conductivity and lattice density. A higher slope of the curve indicated a higher density.
Farag et al., [66]	Effect of surface roughness on defect detection *via* ECT	PBF-LB	316 L SS and Ti-6Al-4 V	50 × 50 mm^2 samples with surface roughness between 8 μm to 11 μm; **1).** notches (0.07 mm width and 25 mm length). **2).** subsurface blind holes (0.17 to 0.3 mm radius).	Commercial Absolute and Reflection EC-probes (both in sweep mode)	Absolute EC (f = 28 KHz, current = 0.0148, and voltage = 5 V). Reflection EC (f = 2 kHz, and voltage = 12 V). For both EC probes: δ = 3 mm	The absolute probe is best for notch detection (0.07 mm width and 25 mm length). Meanwhile, the reflection probe performed best for blind spherical hole (~ 0.2 mm diameter) detection.

(*continued on next page*)

Table 1 (*continued*)

Reference	Focus	AM type(s)	Material(s)	Defect type(s)	Sensor type/method(s)	Optimal/tested parameter(s)	Finding(s)
Kobayashi et al., [108]	Artificial defect identification	PBF-EB	Co-based alloy	Flat bottom holes with diameters of 0.5 mm, 1.0 mm, and 1.5 mm, located at depths of 0.5 mm, 1.0 mm, and 1.5 mm from the top surface.	Differential EC- probe.	f = 250 kHz, Φ = 90 °	ECT's detectability for inner defects increases significantly when the depth of the defect matches the penetration depth. Inner defects with a diameter of at least 0.5 mm and located 0.5 mm deep were reliably detected with a signal-to-noise ratio (SNR) of 2 or higher at a frequency of 250 kHz.
Spurek et al., [111]	Relative Density Measurement *via* ECT	PBF-LB	316 L SS and AlSi10Mg	Real pores in test components	Absolute type EC-probe with a 3-mm diameter ferrite core (UPEC tester by the Sensima Inspection SARL)	316 L SS δ = 945 μm, Φ = 69° AlSi10Mg δ = 313 μm, Φ = 79° Both f = 201.6 kHz, d = 0.5 mm	**1).** A statistically significant and robust correlation was established between relative part density and the ECT signal component, primarily influenced by electrical conductivity (316 L: r (8) = 0.998, $p < 0.001$; AlSi10Mg: r(8) = 0.992, p < 0.001). **2).** Relative density measurement uncertainty *via* ECT was 0.02 % and 0.06 % for 316 L AlSi10Mg respectively.
Kasa et al., [112]	Relative Density Measurement *via* ECT	PBF-LB	AlSi10Mg	Real pores in 5 square samples (100 × 80 × 10 mm^3)	An HTS-SQUID gradiometer module made by SUSTEC, combined with ECT probes consisting of a separate differential excitation ferrite coil and a differential pickup coil.	f = 1.6 kHz, Current amplitude = 20 mA, δ = 2.5 mm, d = ~1 mm, Scan speed = 30 mm/s, and Step size = 2 mm	**1).** Qualitatively distinguished dense AlSi10Mg using colour contour maps of measured voltage amplitude. **2).** The edge effect around the corners of the sample was significant.
Spierings et al., [113]	Relative Density Measurement *via* ECT	PBF-LB	316 L SS	Real pores in 10 cubic samples (25 × 30 × 10 mm^3)	Absolute type EC-probe with 3-mm diameter ferrite rod (UPEC tester by the Sensima Inspection SARL	f = 200 kHz, δ = 945 μm	Achieved a strong correlation (r^2 = 0.997) between the relative density by Archimedes and the EC sensor signal.
Hippert, et al., [110]	Porosity and delamination due to thermal stresses.	PBF-LB	316 L SS	Different sized holes	Isotropic sensor with shielded pod core of 4 mm diameter	**1).** f = 50 kHz and δ = 1.8 mm for porosity. **2).** f = 84 kHz and δ = 1.4 mm for delamination	The colour gradients of the impedance plane contour highlighted areas of porosity and delamination: dark spots indicated metallurgical bonding and no porosities, while whiter spots indicated the presence of porosities and areas of delamination.
D'Accardi et al., [109]	Defect detection *via* ECT	PBF-LB	316 L SS	Porosities from keyhole mode and lack of fusion defects	Two (2) Absolute type EC-probes with 1.6 mm and 0.5 mm diameter cores (ELOTEST B1 V4)	Excitation current = 200 mA. Probe 1: δ = 1.1 mm at f = 200 kHz. Probe 2: δ = 0.7 mm at f = 500 kHz,	**1).** Successfully detected the effects using the amplitudes of the Y-channel **2).** Directional absolute probe is best for Spherical defect detection due to enhanced contrast-to-noise ratio (CNR) values. **3).** Non-directional absolute probe is best for non-spherical defect (lack-of-fusion) detection.
Gruber et al., [114]	Effect of sample thickness and surface quality on the measured electrical conductivity.	PBF-LB	**1).** Deoxygenated oxygen-free pure copper (Cu-OF) **2).** Oxygenated electrolytic tough pitch copper (Cu-ETP)	3 cubes (10 × 10 × 15 mm) 5 rectangular walls (20 × 20 mm, and 500–3 mm thickness) 12 cylinders (8 mm diameter × 43 mm height)	Isotropic sensor (SigmaScope 350)	f = 120 kHz, δ = 190 μm	A polished surface area of at least 15 × 15 mm and a sample thickness of at least 1.5 mm is required, to ensure accurate and reproducible measurements of the electrical conductivity of Copper using the eddy-current method.

(*continued on next page*)

Table 1 (*continued*)

Reference	Focus	AM type(s)	Material(s)	Defect type(s)	Sensor type/method(s)	Optimal/tested parameter(s)	Finding(s)
Barrancos, et al., [115]	EC- probe design and readout electronics development, for *in-situ* PBF-LB monitoring.	PBF-LB	316 L SS	3D hexagonal lattice Open holes of 0.8–32 mm diameter and depths of 0.1–0.8 mm.	Array of 16 AISC-0805F-680J-T EC coils.	$f = 1$ MHz, $\Phi = 15^{\circ}$ $d = 0.4$ mm, Pitch = 5 mm, Step size = 0.1 mm, and Scan speed = 1 mm/s.	**1).** Demonstrated suitability of off-the-shelf wire-wound, ferrite-cored inductors (AISC-0805F-680J-T) for array EC design. **2).** Implemented an adjustable, single-phase demodulation scheme to reduce the complexity of the demodulation circuit, with negligible impact on the imaging results. **3).** Successfully evaluated conductivity changes in the samples.
Eisenbarth et al., [116]	Sub-surface QR code/artifact detection, for authentication and anti-counterfeiting applications	PBF-LB and PBF-ED	316 L SS	15 rectangular samples (27.5 × 7.5 mm and thickness of 3.6 mm)	N/A	PBF-LB sample (f = 521 kHz) PBF-EB sample (f = 200 kHz)	**1).** In PBF-LB samples, individual detection of small pores was not feasible; however, estimation of the average porosity of an area is possible. **2).** Code detection was easier in PBF-EB samples due to differences in magnetic permeability. Specifically, magnetically soft steel, locally mixed with paramagnetic steel in the melt pool, facilitated detection compared to 316 L SS
Yusa et al., [107,117]	Defect detection *via* ECT	PBF-LB	316 L SS	**1).** Branching flaws **2).** Rectangular slits of 5 mm depth and 20 mm length. **3).** Inverse-V shaped notches	Absolute type EC-probe with 3.2 mm diameter core (aect2000N)	$f = 25$ kHz, $d = 0.2$ mm, $\Phi = 45^{\circ}$	Was able to distinguish between regular defects and branching defects. Branching increased eddy current signals.
Bento et al., [118]	Probe design for layer-by-layer detection	DED (WAAM)	Aluminium	Rectangular hole	Custom differential-type Ionic EC probes	$f = 2$ and 3 KHz, $d = 1$ to 5 mm, gain = 90 dB, driving voltage = 12 V	Detected 350 μm defects up to 5 mm depth; at lift-off distance of 5 mm
Todorov et al., [119]	Artificial defect detection and lack-of-fusion defects	PBF-LB	carbon steel 4140	Two (2) notches and six (6) strips of different dimensions	Array eddy current (AEC) consisting of 32 optimized EC coils	$L = 200$ μm; Four (4) $f = 0.125$, 0.25, 0.5, and 2 MHz (total of 124 EC channels)	Detected defects at depths up to 40 μm.

Note: The research articles listed in Table 1 are intended to offer the reader a concise tabular summary of essential EC test parameters, focus areas, findings, and the demonstrated applicability of *ex-situ* ECT exclusively on metal AM components.

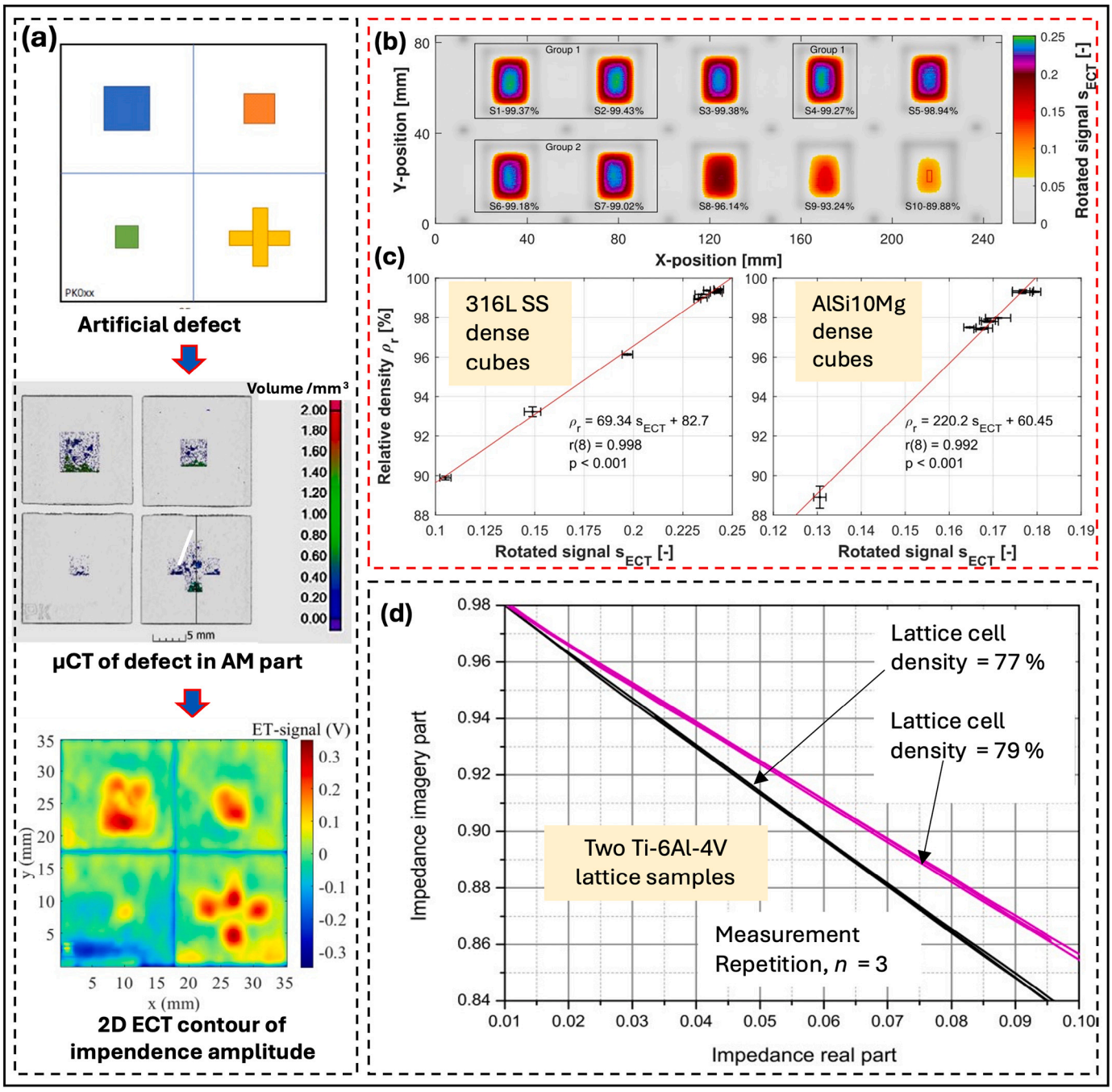


Fig. 7. (a) Comparative 2D *ex-situ* ECT impedance signal contours of artificial defects and μCT data (adapted from D'Accardi et al., [109]); (b) 2D ECT sensor signatures (heatmaps) of relative densities of ten PBF-LB processed 316 L SS test coupons [111]; (c) linear correlation of EC-measured electrical conductivity to relative densities of PBF-LB processed 316 L SS and AiSi10Mg samples [111]; and (d) Linear curves with two distinct slopes, each measured three times, corresponding to theoretical relative densities (percentage of cells) of 77 % and 79 %. These were observed in two cubic lattice specimens PBF-LB processed using TiAl6V powders [84].

the authors observed a high standard deviation ($n = 6$) and a 34.6 % deviation from the ideal bulk electrical conductivity of 100 % IACC when estimating electrical conductivity using ECT. Therefore, they noted that a minimum sample thickness of 1.5 mm was necessary for consistent and accurate measurements of electrical conductivity using the EC method.

Notably, the maximum %IACS values from the bulk conductivity could not be measured by using the EC method. This underscores the challenges in accurately assessing electrical conductivity in metal AM components due to the inherent surface roughness.

3.3. *Ex-situ* ECT for sub-surface temperature estimation

During a typical PBF processing, the part surface temperatures increase with number of build layers shown in Fig. 8b (*i.e.*, build height). This has been observed and reported by Refs. [120, 121] for the PBF-LB processing of Nickel-Titanium alloys (NiTi or Nitinol), and AlSi10Mg [122] samples. Meanwhile changes in electrical conductivity due to heat (temperature) are a known factor affecting the response of EC signals. However, Mukherjee et al. [123] explored this phenomenon as an opportunity rather than a limitation. They leveraged the variations in electrical conductivity due to heat, to monitor sub-surface temperatures

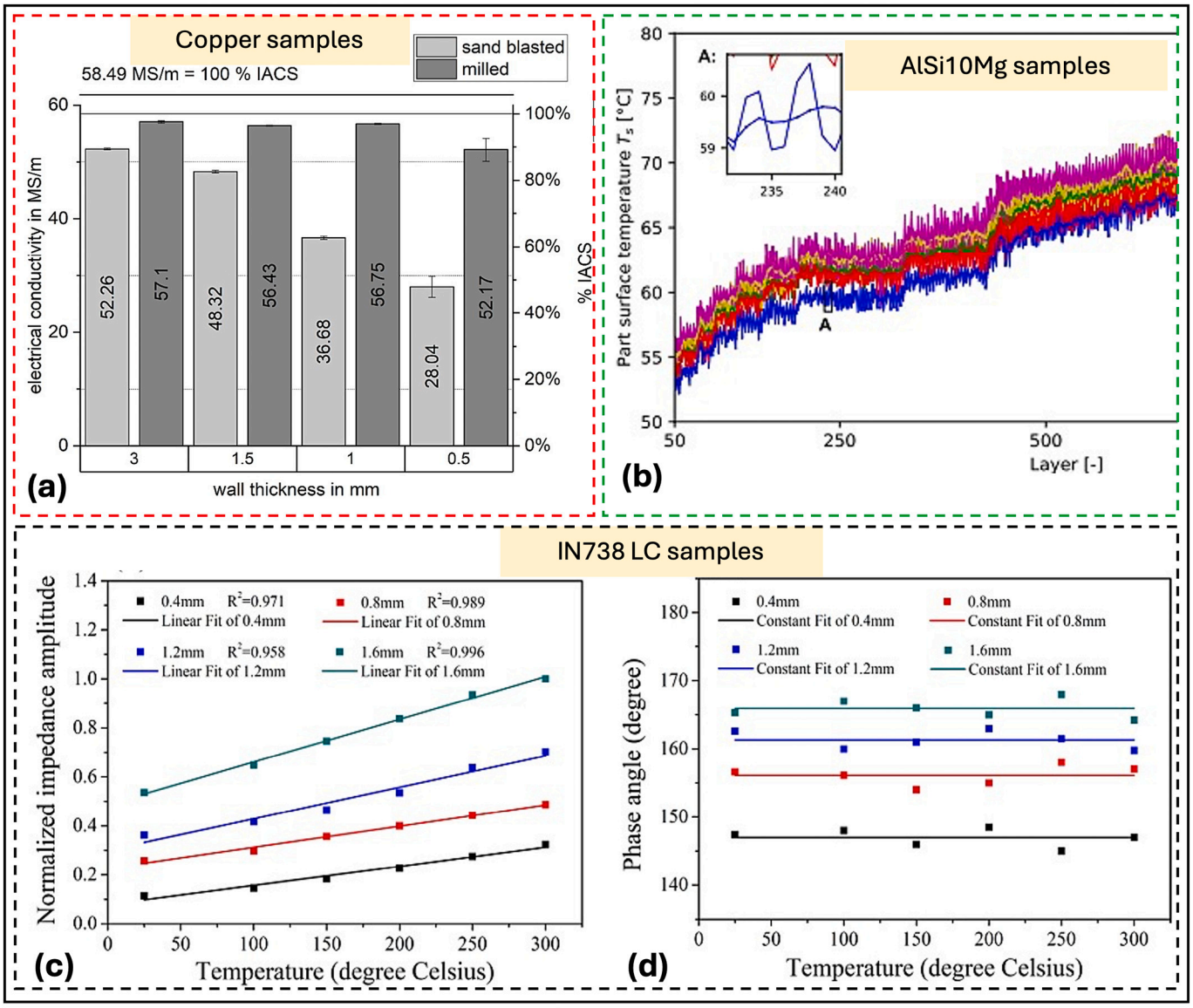


Fig. 8. (a) Effect of surface condition on the measurement of electrical conductivity in PBF-LB processed copper samples using ECT [114]; (b) increase in part surface temperature with number of build layers during PBF-LB processing of AlSi10Mg [122]; Influence of part surface temperature on (c) the normalized impedance amplitude, and (d) EC phase angle of Inconel 738LC samples heated between 25 and 300 °C [60].

using ECT.

To investigate this, they conducted experiments on a 100 × 75 × 1.85 mm aluminium plate by heating it from one side with a controlled heat source, while an EC probe monitored the temperature from the opposite surface. The *ex-situ* ECT setup consisted of a Nortec 600D EC reader with a core diameter of 12.5 mm, excited at a frequency of 2 KHz to achieve a standard depth of penetration of 1 mm. The initial temperature of the heat source was set at 300 °F (~148.9 °C), with increments of 50 °F (~10 °C). The authors observed a near-linear relationship between the measured peak EC-coil voltage and the temperature of the heat source. This increase was attributed to the decrease in sample conductivity and subsequent increase in resistivity with rising temperature. Similarly, Guo et al., [60] reported a linear relationship between the impedance amplitude and surface temperature of ASHM-processed Inconel 738LC heated from 25 to 300 °C. However, the phase angles were relatively unaffected by temperatures as shown in Fig. 8c – d.

By the foregoing, the EC-coil voltage and impedance amplitude can serve as effective indicators of temperature. When appropriately calibrated for the metal alloy type and other ECT parameters optimized, they hold the potential for accurately estimating temperature. This capability can be particularly advantageous for *in-situ* EC monitoring of sample surface temperature during processes like PBF-LB or PBF-EB. However, as noted earlier, the surface temperatures during PBF processing change with build height (refer to Fig. 8b**).** This necessitates further investigation to compensate for this effect (further discussed in **Section 4.4).**

3.4. Ex-situ ECT of metal AM components using giant magnetoresistive (GMR)-based sensors

The aforementioned studies on *ex-situ* ECT in metal AM (**Sections 3.1** to **3.3**) used coil-based isotropic or multi-frequency EC- sensors, which have notable spatial resolution limitations. Close-packed coil-based ECTs opposing signals and fast switching or multiplexing between the coils can also be challenging due to higher induced inductance [124]. Owing to these reasons, giant magnetoresistive (GMR)-based sensors (previously discussed in **Section 2.9**) which are smaller in size

and superior in spatial resolution (compared to coil-based EC sensors [94]), have been investigated for metal AM component assessments.

In an *ex-situ* ECT setup, Ehlers et al., [69] explored the effectiveness of using GMR-based sensors to analyse artificial sub-surface defects of μm length-scale in PBF-LB processed 316 L SS component. The GMR array comprised 32 sensor elements positioned near the edge of the GMR chip. The ECT setup employed the GMR module in a Wheatstone bridge configuration, with one frequency generator generating excitation coil current at a frequency (f_1), and another generator providing bias voltage at another frequency (f_2) for the Wheatstone bridge. The use of two frequencies, f_1 and f_2, generated heterodyne frequencies (f_3) which enhanced the sensitivity of the GMR-based ECT setup to magnetic fields in the μT range. The heterodyne principle also decreased the sampling rate of the data acquisition system by at least a factor of 50, while minimizing the effects of inductive coupling that is induced by the excitation coils.

3.5. Ex-situ ECT for metal powder characterization

Metal powder characterization plays a crucial role in metal AM, influencing the quality and properties of the final printed components. Understanding and characterizing these powders are crucial for ensuring the integrity and performance of the final AM components. Although the application of *ex-situ* eddy current testing (ECT) for powder characterization is underexplored, the study by Haddad and Zergoug [125] highlights its potential, particularly in assessing powder bed characteristics for elementally (mechanically) mixed high-entropy alloys (HEAs). HEAs, such as the equiatomic face-centred cubic (FCC) CoNiCrFeMn alloy (commonly known as Cantor alloys) [126], are composed of five or more principal elements in roughly equal proportions (typically 5–35 atomic percent each). Recent definitions have expanded to include alloys with as few as three principal elements, with maximum element concentrations exceeding 35 atomic percent [127].

Haddad and Zergoug [125], investigated the feasibility of using ECT to characterize $Fe_{(1-x)}$ Co_x, Fe, $Fe_{80}Ni_{20}$, and $Cu_{70}Fe_{18}Co_{12}$ metal powder characteristics, focusing on properties such as density, grain size (diameter), and structural attributes. The powders were subjected to mechanical mixing using a planetary ball mill. The powders were mechanically processed using a planetary ball mill and examined at various stages of milling, ranging from 2 to 100 h. ECT measurements were conducted using an Agilent 4284 A impedance analyzer programmed to operate at excitation frequencies between 50 Hz and 500 kHz. By correlating impedance data obtained through ECT with X-ray diffraction (XRD) analyses, the study revealed a clear relationship between impedance variations and the crystallographic evolution of the powders over the milling process. These findings underscore the potential of ECT as a non-destructive tool for monitoring the structural and compositional changes in metal powders, providing insights into their suitability for AM applications.

3.6. Finite element analysis (FEA) in ex-situ ECT

FEA simulation is a powerful tool for understanding and analyzing the behaviour of ECT systems. Applications of FEA in ECT include:

1. Predictive modeling of the electromagnetic fields generated during eddy current testing,
2. EC probe or coil design optimization (by simulating different probe geometries, sizes, and configurations, to determine the most effective setup to detect specific defects of interest),
3. Parameter sensitivity analysis, by considering the effects of excitation frequency, lift-off distance, and material properties, and
4. Validation against experimental data to ensure their accuracy and reliability

The governing equation for a typical EC-FEA takes the general form [128];

$$\left(\frac{j\omega}{\rho-\omega^2\varepsilon}\right)\boldsymbol{A}+\nabla\times\frac{\nabla\times\boldsymbol{A}}{\mu_r\mu_0}=\boldsymbol{J_e} \tag{9}$$

where j, ε, ω, ρ, represent the imaginary unit, the permittivity of the material, the angular frequency of the alternating current, and the electrical resistivity of the material, respectively. ∇, μ_0 and μ_r, represent the gradient operator, the permeability of vacuum, and the relative permeability of the material, respectively. $\boldsymbol{A}$ and $\boldsymbol{Je}$ refer to the magnetic vector potential (MVP), and eddy current density, respectively.

The computation of impedance, Z is mathematically expressed as a function of the MVP;

$$Re(Z)=-\frac{N^2}{J_eS^2}\omega\iint_s 2\pi Im(A)ds \tag{10}$$

$$Im(Z)=-\frac{N^2}{J_eS^2}\omega\iint_s 2\pi Re(A)ds \tag{11}$$

where $Re(Z)$ and $Im(Z)$ represents the real and imaginary parts of the impedance, N represents the number of turns in the coil, and S is the cross-sectional surface area of the inductor coil. $\iint_s$ represents the surface integral over the coil's surface area, while $I\,m\,(A)$ and $Re(A)$ refer to the imaginary and real parts of the magnetic vector potential (A). More details on mathematical formulations of EC-FEA can be found in Refs [95,128–130].

Fernandez et al., [79] used FEA to accurately model the transient magnetic behaviour of PEC systems, allowing for the analysis of the decay rate of signals in relation to the wall thickness of the component and the effects of probe lift-off. Yusa et al., [107,117] utilized the COMSOL Multi-Physics platform to address uncertainties regarding the exciting current and signal phase origins in their experiments using an absolute-type pancake EC probe.

Specifically for defect detection in PBF-LB processed 316 L SS and Ti-6Al-4 V parts using an absolute EC probe, Farag et el., [66] utilized ANSYS Maxwell to predict and differentiate between a sphere (D = 3 mm) and notch sub-surface defect (at 10 mm surface) effects on the EC-probe impedance responses. A spherical defect has a larger volume compared to a notched defect, which results in a larger area of disturbed eddy currents around the spherical defect with a continuously changing dimension vis a *viz.* its circumference. This larger area of disturbed eddy currents results in a more complex impedance response, leading to double impedance peaks in the simulated EC signal (**Fig. 9**a). Such double impedance peaks in spherical defects were also observed in the FEA analysis by Belkacem et al., [80] using Computer Simulation Technology (CST) Studio Suite 2020. On the other hand, a modelled notched defect with a smaller surface area produced a single senor response peak. This results in a less complex impedance response with a single impedance peak (**Fig. 9**b).

Bento et al., [118] utilized Finite Element Analysis (FEA) to optimize the design of their custom EC probes for assessing metal components produced through Wire Arc Additive Manufacturing (WAAM), a type of DED technique. These components have large layer thicknesses compared to PBF and typically feature curved surfaces that interfere with conventional EC probes, such that defects in the WAAM components are barely detectable. To address this issue, the authors designed the probe shape using ANSYS® Maxwell 3D software, modelling it based on the curvature of weld beads found in WAAM parts. The test specimen, representing an aluminium bar (AA 6082-T6) with high electrical conductivity, was subjected to an excitation frequency of 2 kHz. The FEA aimed to elucidate the electromagnetic behaviour and response of the custom-shaped EC probes at a specific lift-off distance from the curved weld bead surfaces of a WAAM-processed aluminium bar, which contained a sub-surface artificial defect (a rectangular notch). The analysis

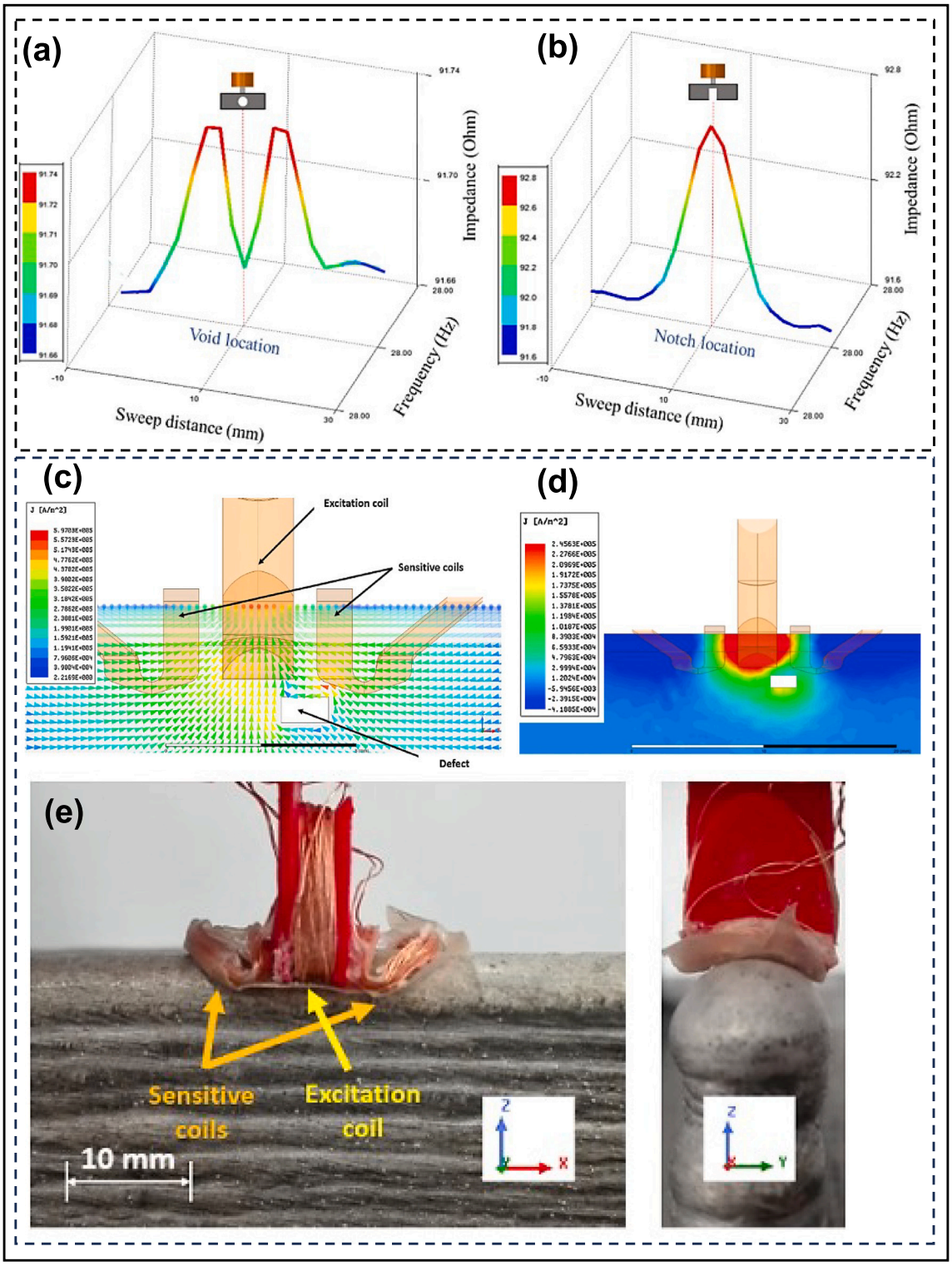


Fig. 9. Eddy current finite element predictions of: (a) Probe impedance response due to spherical defect, and (b) square notch in a 316 L SS test sample [66]; (c) vector field ($\boldsymbol{J}_e$), and (d) magnitude of the Y component of vector field ($\boldsymbol{J}_e$) from the XZ Plane of curved surface of an aluminium bar, with curved surface similar to the surface curvature of WAAM components (e).

revealed that the current density vector field (J) on the bar's surface was affected by the presence of the defect, as depicted in Fig. 9b. Specifically, the magnitude of the J component in the XZ plane had positive values (depicted in red to light-blue colours in Fig. 9c) beneath the excitation coil and negative values (shown in darker blues) farther away. This indicates a reversal in the direction of the J vector as it moved away from the excitation coil in both the X and Z directions. Fig. 9d shows corresponding images of the actual WAAM aluminium sample and the EC probe to the FEA results. Overall, the FEA results suggest that modifying the shape of the IOnic EC probes to accommodate the curvature of WAAM beads is effective for accurate assessment in such scenarios. Note that actual *ex-situ* ECT parameters using the final probe design are summarised in Table 1.

4. *In-situ* eddy current sensing and monitoring of metal AM

The layer-wise methodology intrinsic to metal AM processing offers the prospect for *in-situ* monitoring of surface and sub-surface features using EC, carried out on a layer-by-layer basis as the build progresses. By mounting the EC-sensors on the re-coater arm, precise control over lift-off can be achieved and the EC data acquisition rate can be synchronized with re-coater arm movement and speed. Thereby, enabling and enhancing the *in-situ* ECT performance without significant modifications to the AM equipment. An exemplary block diagram for integrating *in-situ* EC sensors to OEM PBF equipment is shown in **Fig. 10**a – b. Unlike conventional *ex-situ* ECT of whole or bulk metal components, detecting deep volumetric discontinuities is limited due to material skin depth phenomena (as discussed in **Section 2.1)** [77,131,132]. The layer-wise manufacturing process of DED and PBF AM techniques results in melt layer thicknesses in the sub-millimetre and micron length scales, respectively. Therefore, employing EC for *in-situ* defect detection of sequential few-micron- or millimetre-sized layers reduces the dependence of ECT accuracy on the material skin depth factor to a certain degree. This facilitates physical property monitoring and deep volumetric discontinuity tracking within the AM component during fabrication (*i.e.*, *in-situ*).

In a conventional EC setup, the upper-speed limit for effective operation with an eddy current detector is typically around 150 mm/s [46]. This speed is within the operational range of typical powder spreader or re-coater mechanisms in commercial PBF-LB and PBF-EB systems. For example, according to the Aconity*MINI*® PBF-LB manual/documentation [6], the default setting for the *'Return velocity*,' which dictates the velocity of the slider (re-coater) as it returns to the powder supply, is set at 250 mm/s (range: 1 to 2500 mm/s). However, users have the option to adjust this velocity as needed. By optimizing the re-coater *'Return velocity'* and EC sensor in tandem, it becomes feasible to employ a sweep mode scan during the EC scan pass, further enabling the acquisition of more information across the process plane. Note that the ideal EC scan direction is the return direction of the re-coater arm towards the powder bed (see **Fig. 10**a).

The sweep EC scan mode facilitates a thorough examination of the test piece by systematically scanning the entire sample within the process plane (**Fig. 10**b). During this process, the deviation of the EC signal is recorded and analyzed over time in relation to the central reference horizontal axis [48]. Given the right-sized EC-probe type or array of EC probes, the sweep mode ensures that all components on the AM build platform are within the effective EC sensing area inspected, and EC data is collected continuously in one scan pass, to create a detailed signal map of the AM build. Previous studies that have used single coil EC probes in sweep mode are [46,48,66].

Based on the context of the above discussion, eddy current sensing or monitoring (ECS or ECM) is deemed more fitting for *in-situ* AM monitoring description than ECT. However, *in-situ* ECM will be utilized throughout the remainder of this article. The potential of *in-situ* ECM in metal AM has caught the attention of researchers, AM technology magazines like www.metal-am.com [133], and AM metrology OEMs such as AMiquam® (AMiquam SA, Gland, Switzerland - www.amiquam.net). However, this research area is still in its early stages of development with fewer than 10 research articles published to date specifically focused on *in-situ* ECM for Metal AM. A summary of these *in-situ* studies is provided in Table 2.

4.1. *In-situ coil-based ECM for detection of artificial defects and re-coater blade scraping*

The team of researchers at Engineering With Industry (EWI), Ohio, USA (www.ewi.org) led by Todorov et al., [119] in 2018 published possibly, the first demonstration of *in-situ* ECM for the detection of defects in IN625, duplex stainless steel 2205, and carbon steel 4140 processed *via* PBF-LB. They developed an array eddy current monitoring (A-ECM) system, comprising 32 optimized coil elements (**Fig. 11**a-1), with a sensor lift-off set at 0.2 mm (200 μm), as per their patent-pending design. All 32 coils were simultaneously excited at frequencies of 0.125, 0.250, 0.500, and 2 MHz, providing 124 eddy current data channels. The resolution along the scanning direction was 0.1 mm, while the Y-axis resolution was 0.826 mm, determined by the array design and coil diameter. During the *ex-situ* trial run, the researchers successfully detected 0.1 mm and 0.2 mm deep notches (*i.e.*, engineered defects) in duplex stainless steel 2205 and carbon steel 4140 test specimens. They reported that the A-ECM signal intensity exhibited a strong correlation with the depth of the flaw, enabling the identification of shallow flaws with depths comparable to the thickness of a single AM layer, approximately 0.04 mm (*i.e.*, 40 μm).

For the *in-situ* ECM trials by Todorov et al., [119], the A-ECM sensor was attached to the re-coater arm of an experimental PBF-LB test bed, with the buffer circuit housed within the enclosure. The data logger was positioned outside the chamber, and the data acquisition rate was configured at every 0.1 mm. The substrate was pre-heated to 100 °C for the PBF-LB processing of a 20 × 20 mm demonstration specimen using IN625 alloy powder. The layer thickness was set at 0.04 mm, and both volumetric defects (vertical holes) and planar defects (horizontal notches) were included within the build CAD file to simulate lack-of-

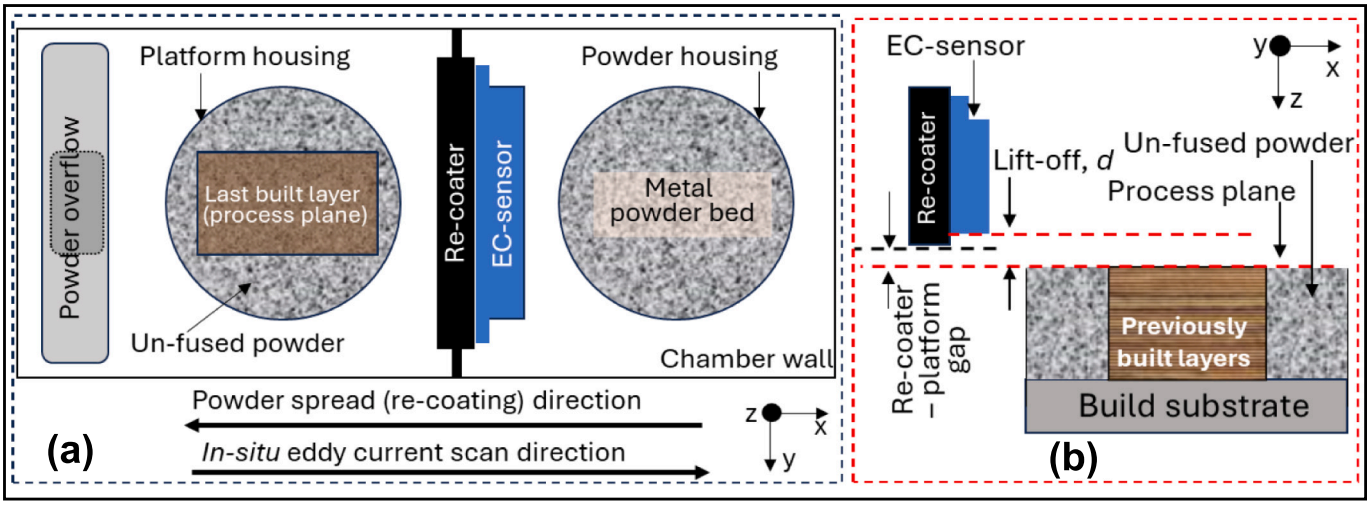


Fig. 10. (a) Top elevation block diagram of preferred *in-situ* eddy current (EC) sensor integration unto the re-coater arm of a PBF-LB equipment (© Authors); (b) front elevation block diagram showing the working distance between the part surface and the integrated EC- sensor (© Authors).

Table 2
Overview of *in-situ* eddy current testing of metal AM components.

Reference	Focus	AM type	Material (s)	Defect type	Sensor type/ method(s)	Optimal/tested parameters	Finding(s)
Todorov et al., [119]	Artificial defect identification	PBF-LB	IN625	Horizontal LOF defects of L = 5 mm x W = 5 mm at D = 0.08 to 0.4 mm. 5 vertical LOF defects (holes) with 0.09, 0.18, 0.27, 0.45, and 0.9 mm diameter and depths up to 0.73 mm. Process-induced pores (real-defects).	Array eddy current module (A-ECM) consisting of 32 optimized EC coils	L = 0.2 mm Simultaneous frequency excitation at f = 0.125, 0.25, 0.5, and 2 MHz Acquisition rate = 0.1 mm	**1).** Identified surface and subsurface defects, including narrow features mimicking vertical and horizontal lack of fusion (LOF), subsurface LOF, variations in surface topography, and localized changes in bulk electromagnetic properties **2).** Detection of re-coater arm scraping adds an advanced capability for process monitoring using *in-situ* ECM.
Zimermann, et al. [134]	Artificial defect identification	DED (WAAM)	Ti-6Al-4 V	Two tungsten balls (diameters, D = 3 mm and 2 mm); and Two tungsten tubes (L = 30 mm, Inner-D = 1 mm, and Outer-D = 3 mm); Both tungsten artifacts were embedded in a 250 mm long by 25 mm wide Ti-6Al-4 V wall.	N/A	Surface temperature = 180 to 230 °C; Scan speed = approx.. 14.71 mm/s (17 s to scan 250 mm); Acquisition rate = 500 Hz; f = 50 kHz; 40 dB of gain; and voltage excitation of 2.5 V.	This study successfully detected artificial tungsten reflectors up to 4.5 mm deep (second uppermost layer), but natural porosity defects identified by Xray-CT were undetected.
Sallem et al., [135]	Machine Learning (ML)-enabled porosity prediction.	PBF-LB	Ti-6Al-4 V	Ten (10) plates measuring 15 mm × 15 mm × 20 mm	AMiquam ECM with two channels.	$\delta \approx 1.49$ *mm*	Convolutional Neural Network (CNN)-based algorithms demonstrated effective layer-by-layer prediction of porosity defects, achieving a mean absolute error (MAE) of; **1).** 0.1 % with the CNN2D algorithm; and **2).** 0.11 % with the Long Short-Term Memory (LSTM) CNN algorithm.
Spierings et al., [113],	Real flaw detection	PBF-LB	316 L-SS	Ten (10) cubic samples with a size of 25 mm × 30 mm × 10 mm	AMiquam ECM with two channels.	*N/A*	2D EC contour plots in the XZ-plane revealed sections along the build height containing flaws.
Spurek et al. [47]	Relative Density estimation	PBF-LB	AlSi10Mg	Five (5) cubic samples with dimensions 10 mm × 10 mm × 12 mm.	Instrument: Ultra-Portable Eddy Current (UPEC) instrument by Sensima Inspection Sarl, Gland, Switzerland. Sensor: Ferrite pot core coil with Inductance = 80 μH and Outer diameter = 5.8 mm	f = *200 kHz;* δ = 313 μm; $\sigma_{(AlSi10Mg)}$ = 12.85 MS m − 1; $\mu r_{(AlSi10Mg)}$ = 1.00; sampling rate = 375 Hz; L = 500 μm	**1).** ECT *vs.* μCT: ECT-measured final part height aligns well with μCT measurements, indicating lift-off can monitor part height and vertical deformations during manufacturing. **2).** Layer-wise relative electrical conductivity strongly correlates (r = 0.87) linearly with relative density measured *via* μCT. **3).** Regression Analysis showed that layer-by layer relative density can be measured from EC-data with a mean absolute error of 0.126 %.
Spurek et al., [122]	Process-induced temperature influence on *in-situ* monitoring of relative density using ECM	PBF-LB	AlSi10Mg	Five (5) cubic samples with dimensions 10 mm × 10 mm × 12 mm.	Instrument: Ultra-Portable Eddy Current (UPEC) instrument by Sensima Inspection Sarl, Gland, Switzerland.	f = *200 kHz;* δ = 313 μm; $\sigma_{(AlSi10Mg)}$ = 12.85 MS m − 1; $\mu r_{(AlSi10Mg)}$ = 1.00; sampling rate = 375 Hz; L = 500 μm	**1).** The ECT response varies linearly with part temperature, as an increase in surface temperature decreases measurable electrical conductivity. **2).** Inter-layer temperature

(*continued on next page*)

Table 2 (*continued*)

Reference	Focus	AM type	Material (s)	Defect type	Sensor type/ method(s)	Optimal/tested parameters	Finding(s)
					Sensor: Ferrite pot core coil with Inductance = 80 μH and Outer diameter = 5.8 mm		varies between 55 °C to 75 °C irrespective of the part position on the build plate and the applied process parameters. **3).** Layer-to-layer differences of 0.15 % relative density can be detected *via* ECT. **4).** Induced temperature variations due to varying VEDs have a negligible impact on the final part temperature and overall temperature variation during the build process when *in-situ* ECT measurements are conducted. This is due to the high cooling rates inherent in PBF-LB processing.
Sergeeva-Chollet et al., [137]	*In-situ* eddy current module development	PBF-LB	AlSi7Mg	A sample block with two stepped sections. The lower step contains seven surface-breaking notches of varying sizes, while the upper step features four embedded notches at different depths. During fabrication, the lower step was covered with powder while the upper step was being built.	Two (2) coils of diameter of 3 mm with overlap and operated in emitter/ receiver separated mode.	*f = 1 MHz; voltage, V = 8 V*	**1).** Surface-breaking defects approximately 100 μm in width can be detected. **2).** Unfused powder surrounding the built component did not impact the signal-to-noise ratio **3).** An excitation frequency of 1 MHz is too high to detect defects located 180 μm below the surface in the fused area. **4).** The study highlighted the necessity of using an array sensor with adequate spatial resolution (MR-based ECM)
Ehlers et al., [138]	GMR-EC development for geometry detection	PBF-LB	316 L-SS	A sample block with five stepped sections, each having progressively smaller areas. During fabrication, the lower step sections were covered with powder while the upper step sections were being built	EC system with 128 MR elements, single-wire excitation, a 125 μm MR pitch, and a total testing width of 16 mm	*f = 1 MHz;* δ = 565 μm; primary excitation frequency (f_1) = 1 MHz; bias voltage frequency (f_2) = 980 kHz produced a heterodyne frequency (f_3) of 20 kHz	The GMR EC array detected sample edges and geometry up to 164 layers (6.54 mm) from the build platform.

Note: The research articles listed in Table 2 provide a concise summary of the limited studies (available and accessible to the Authors, at the time of writing) on *in-situ* ECM for metal AM components, highlighting key EC test parameters, focus areas, findings, and the demonstrated applicability of the technique.

fusion defects. The defects were characterized by deviations observed in both the phase and magnitude of the EC signals. Further confirmation of EC signal perturbations resulting from sample edge and re-coater arm scraping were also observed (see **Fig. 11**a-2). Sergeeva-Chollet et al., [137] also demonstrated that *in-situ* ECM can detect defects as small as 0.1 mm (~ 100 μm) in width embedded in AlSi7Mg samples, using perturbations in the EC signal magnitude (μV). However, they reported that the detectability also depended on the defect height. Defects with a width of 3 mm and 2 mm were detected at heights >0.16 mm, while thinner defects (0.5 mm wide) were detectable only at heights >0.6 mm.

This initial investigation highlighted the dual potential of ECM for *in-situ* real-time monitoring of re-coater condition (*i.e.*, re-coater arm scrapping during a build) and the as-built component *in-situ* quality. Re-coater arm scraping commonly occurs due to pronounced bulging of the solidified melt layer, which then contacts or interferes with the re-coater blade during powder spreading (re-coating) of a new layer. This pronounced bulging could be caused by thermal stress-induced warpage of the newly solidified melt layer (or entire built part), or surface balling resulting from inappropriate print parameter selection for the specific metal powder and component geometry.

Given the nature of the WAAM process, including more macroscopic dimensions and the need for deposition and/or sample movement, it can be considered that it would be difficult to ensure a constant distance between the sensor and the built surface during production. Nevertheless, Zimermann, et al., [134] demonstrated the applicability of *in-situ* ECM for detecting engineered defects (embedded tungsten rods) in Ti-6Al-4 V test coupons manufactured using the WAAM AM technique. They mounted a pancake-type EC sensor (a flexible EC probe by Eddyfi Technologies, Canada) onto a WAAM deposition robot arm as shown in **Fig. 11**b-1. The EC -system comprised an array of 32 EC coils arranged in two rows of 16. It was programmed to conduct a delayed ECM inspection pass after specified layer depositions using an excitation frequency of 50 kHz, skin penetration depth of ~4.5 mm, and an acquisition rate of 500 Hz. The delayed ECM pass ensured that the temperature of the as-built WAAM component process plane remained below the maximum operating temperature of the EC sensor (< 150 °C). The system gain and

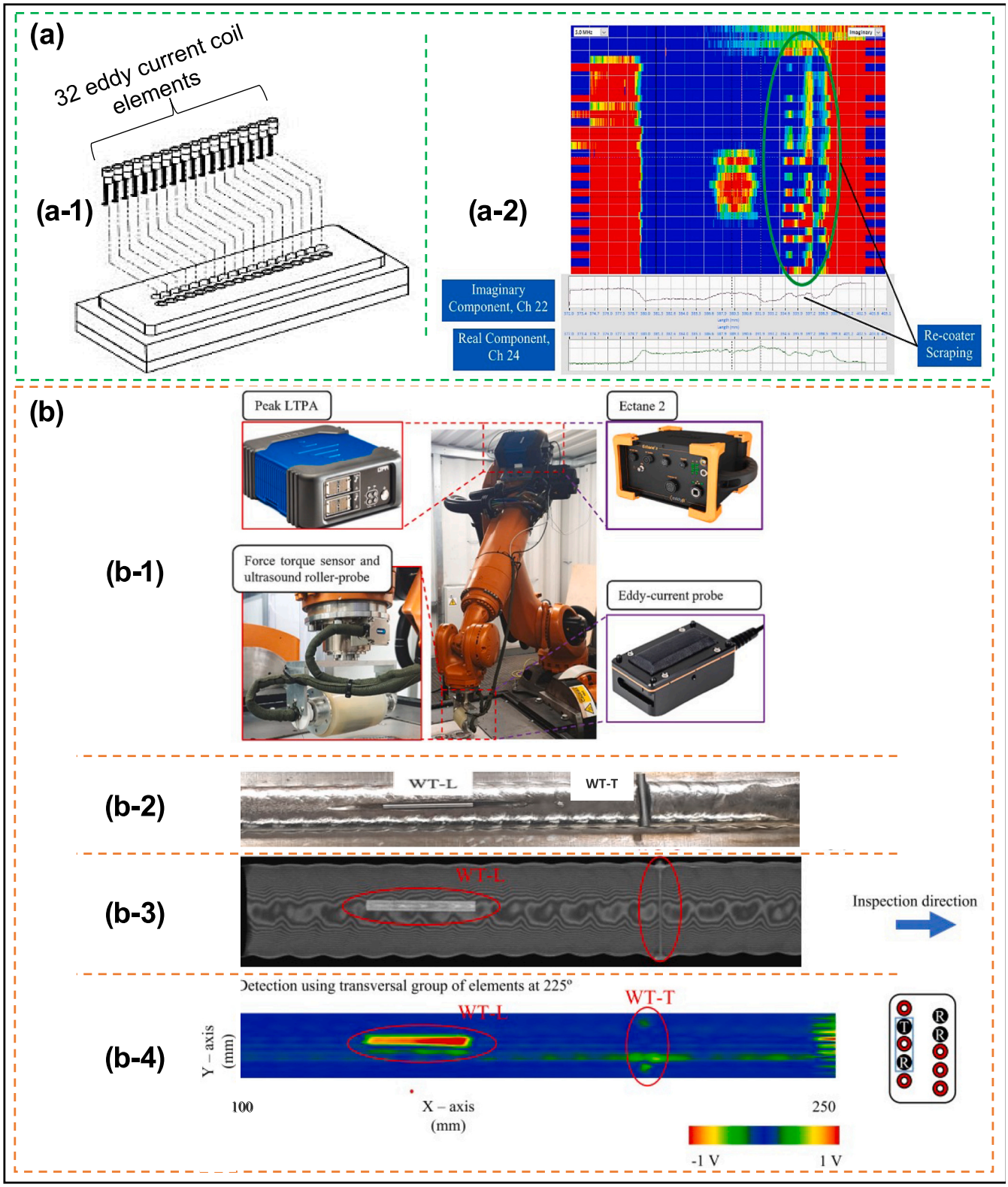


Fig. 11. (a) Illustration of the *in-situ* array eddy current sensor (A-ECS) featuring 32 optimized coil elements (*a-1*); 2D A-ECS signal plots highlighting re-coater scraping events (*a-2*), adapted from Todorov et al. [119]; (b) Retrofitted WAAM deposition robot equipped with ultrasound and eddy current hardware (*b-1*); *(b-2*) Image of two tungsten tubes embedded in a WAAM single track (horizontal WT-L and vertical WT-T) after the deposition of three initial layers; (*b-3*) X-ray computed tomography (CT) scan of the tungsten rods following four additional WAAM passes; and (*b-4*) Eddy current contour plots showing the position of the tungsten rods, adapted from Zimermann, et al., [134].

voltage were configured to 40 dB and 2.5 V, respectively. They noted that two embedded tungsten tubes (WT-L and WT-T shown in Fig. 11b-2 and b-3) were most clearly visible when a transversal group of EC elements with a 225° phase rotation was used, as shown in Fig. 11 b-4.

Due to the limited skin penetration depth beyond the fourth deposited layer, defects located deeper, at approximately 8 mm after the fifth deposited layer, could not be detected. While the study largely succeeds as a demonstration of *in-situ* ECM in WAAM, the authors acknowledged an important limitation; the inability of ECM to detect natural defects (porosities) identified by µCT. This observation highlights the need for further investigation into improving ECM defect detection capabilities.

4.2. *In-situ coil-based ECM for global relative density and layer-wise relative density estimation*

Sallem et al., [135] conducted *in-situ* ECM detection of porosity defects in Ti-6AL-4 V components using an ECM system developed by AMiquam®. This system featured two EC-sensor channels affixed to the powder re-coating mechanism of an SLM Solutions 125 HL PBF-LB machine as shown in Fig. 12. The authors established a correlation between the global relative density due to real pores (porosity) and the average *in-situ* EC signal derived from 20,400 layers of build. Similarly, Spierings et al., [113], also used an AMiquam® *in-situ* ECM system with two EC-sensors, to demonstrate the feasibility of *in-situ* direct part density prediction, with global relative densities ranging from 90 % to 99.5 % in parts from the PBF-LB process. They examined ten 316 L SS samples measuring 25 × 30 × 10 mm^3, manufactured on a Concept Laser M2 machine using varied PBF-LB process parameters.

Similar to the previous study, Spurek et al. [47] demonstrated the utilization and adaptation of *in-situ* ECM to the re-coater arm of an AconityMIDI+ PBF-LB equipment. They employed an Ultra-Portable Eddy Current (UPEC) instrument, manufactured by Sensima Inspection Sarl, Switzerland, with an outer coil diameter (d_c) of 5.8 mm. The *in-situ* ECM setup was operated in absolute mode using an excitation frequency (f) of 200 kHz, a sampling rate (f_s) of 375 Hz, and a nominal lift-off of 500 µm. The re-coater arm speed was set at 100 mm/s. The components underwent µCT analysis, and a segmentation algorithm was developed to spatially divide the µCT data into slices corresponding to the layer-wise ECM data. Subsequently, the relative density of these slices (ρ_s) was determined and correlated with the EC-measured relative electrical conductivity (σ_r) of the AlSi10Mg layers using the regression function in eq. (12). A strong correlation ($r = 0.87$) was reported between the layer-wise acquired σ_r from the *in-situ* ECM system and the relative density of the corresponding material volume measured *via* µCT (Fig. 13a). Further regression analysis indicates that layer-wise relative density $\rho_s(\sigma_r)$ could be measured using eq. (12) with a mean absolute error of 0.126 %.

$$\rho_s(\sigma_r) = 0.9737 \times \sigma_r + 2.3563 \tag{12}$$

As discussed in **Sections 2.4, 3.1** and **3.3,** the accuracy of EC-measurements of electrical conductivity exhibits an inverse correlation with surface temperature, following a linear approximation equation in eq. (5). The increase in surface temperature of parts (residual heat) during PBF processing increases with an increase in built layers (refer to Fig. 8b). This prompts inquiry into how surface temperature might affect *in-situ* ECM signals, which rely on measured relative electrical conductivity for layer-wise relative density estimation. For instance, the linear regression model (eq. (12)) proposed by Spurek et al., [47] for predicting relative density based only on σ_r is suitable for up to ~200 built layers as shown in Fig. 13a. However, as shown in Fig. 13b, significant discrepancies arose between the µCT data and the *in-situ* EC-estimated layer-wise relative densities across build heights consisting of ~1000 layers using eq. (12). Notably, these deviations in EC-estimated $\rho_s(\sigma_r)$ begin around layers 250 and 500. For context, since the layer thickness parameter during the PBF-LB process was 60 µm, the layer-wise $\rho_s(\sigma_r)$ estimation accuracy using *in-situ* ECM become unreliable at build height exceeding ~15 mm (*i.e.*, 15 mm/60 µm ≥ 250th layer).

Subsequent research by Spurek et al., [122] addressed this by examining the impact of part surface temperatures T_s on relative density estimation across larger numbers of build layers. They observed that differences in T_s between layers (*i.e.*, the layer-to-layer temperature difference of ~20 °C) had a more pronounced influence on *in-situ* ECT measurement than part-to-part temperature differences, which were marginal (measuring just 3.4 °C). Their findings showed that the rising temperatures as more layers were fabricated led to a decrease in electrical conductivity (in a linear manner), This error can lead to under or overestimation of the layer-wise relative density using eq. (12). Consequently, they proposed a multiple linear regression function given in eq. (13), which accounts for the effects of σ_r and surface temperature, T_s on layer-wise relative density estimation, $\rho_s(\sigma_r, T_s)$ of AlSi10Mg samples. As shown in Fig. 13c, the layer-wise relative density estimation using $\rho_s(\sigma_r, T_s)$ is much more reliable across the entire 1000 built layers examined (sample dimension was 60 mm height with a build layer thickness of 60 µm). Using eq. (13), layer-wise density prediction accuracy was increased by 15 % compared to eq. (12) without surface

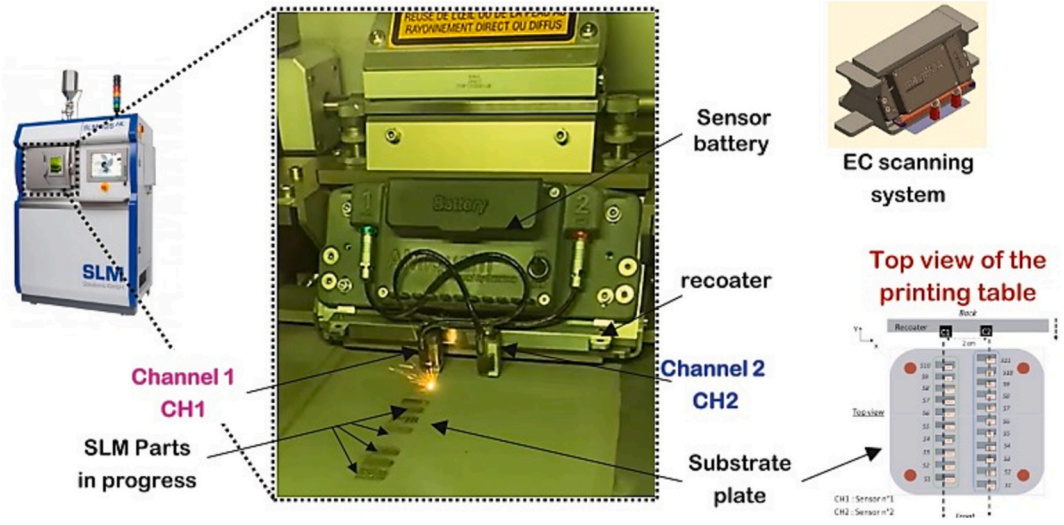


Fig. 12. A retrofitted SLM Solutions 125 HL PBF-LB machine with an *in-situ* ECT system comprising two coil-based EC-sensors (channel 1 and channel 2) made by AMiquam® [135].

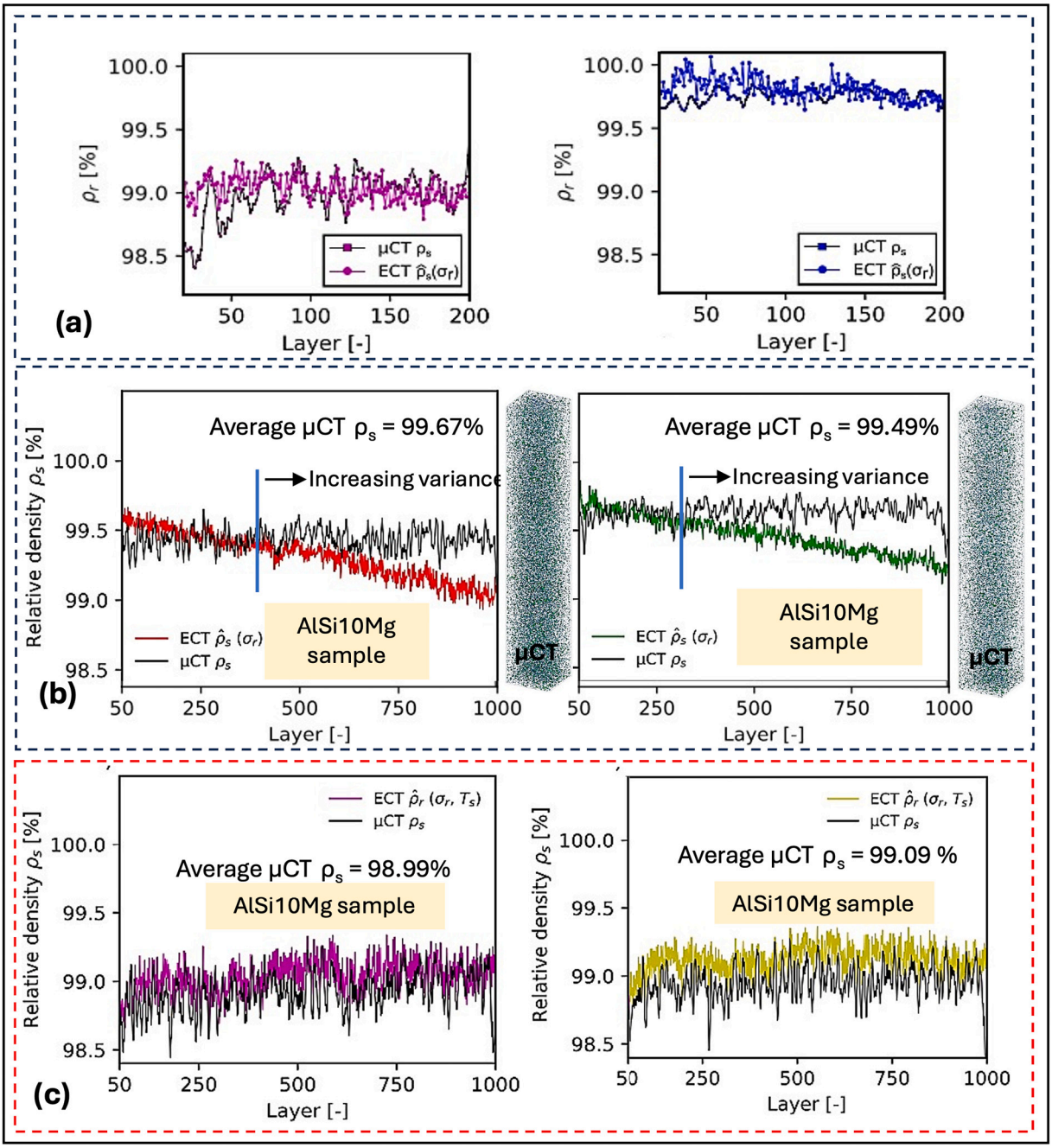


Fig. 13. Layer-wise relative density estimation, $\rho_s(\sigma_r)$ based only on the *in-situ* ECM-measured relative electrical conductivities, σ_r of two AlSi10Mg samples consisting of (a) 200 layers, each having two different μCT-measured relative densities (adapted from Spurek et al., [47]); and (b) up to 1000 layers, each having two different μCT-measured relative densities; and (c) layer-wise relative density $\rho_s(\sigma_r, T_s)$ estimation compensating for part surface temperature, T_s of two AlSi10Mg samples consisting up to 1000 layers, each having two different μCT-measured relative densities (Adapted from Spurek et al., [122]).

temperature, T_s compensation. The average global relative density prediction error $\Delta\rho_r$ for all five samples reduced from 0.154 using eq. (12) to 0.102 using eq. (13), representing an accuracy increase of approximately 33.77 % (see Table 3).

$$\rho_s(\sigma_r, T_s) = (0.0507 \times T_s) + (1.6024 \times \sigma_r) - 63.6758 \quad (13)$$

In both studies by Spurek et al., [47,122], the AlSi10Mg samples with different porosities resulting in the variations in relative densities were achieved by varying the laser scan speed from 1500 to 2100 mm/s, whilst keeping all other PBF-LB parameters constant.

Table 3
Comparison of global relative density predictions of PBF-LB processed AlSi10Mg samples, with and without compensation for part surface temperature (adapted from Spurek et al., [122]).

Part	ρ_r [%]	$\overline{\rho_s}(\sigma_r)$ [%]	$\Delta\rho_r$ [%]	$\overline{\rho_s}(\sigma_r, T_s)$ [%]	$\Delta\rho_r$ [%]
P1	99.94	99.80 ± 0.24	0.14	99.95 ± 0.16	0.01
P2	99.67	99.46 ± 0.14	0.21	99.51 ± 0.11	0.16
P3	99.49	99.31 ± 0.17	0.18	99.25 ± 0.12	0.24
P4	99.09	99.20 ± 0.16	0.11	99.14 ± 0.12	0.05
P5	98.99	99.12 ± 0.16	0.13	99.04 ± 0.13	0.05
Average predictor error:			0.154		0.102

4.3. *In-situ* ECM for monitoring process temperatures

Peng, et al. [136] investigated the potential of *in-situ* ECM for real-time 3D temperature field monitoring during the PBF-LB process. They employed analytical thermal and electromagnetic models, integrating thermal distribution maps into 3D EC numerical models. This allowed them to measure process temperatures using EC-induced voltages and electromagnetic signal features. They determined optimized EC frequencies through experimentally validated electromagnetic simulations. This multi-faceted approach not only sheds light on the complex interplay between thermal and electromagnetic dynamics, but also paves the way for more accurate and reliable real-time AM process monitoring using ECM.

4.4. *In-situ* ECM for analysing the impact of un-fused powder particles

During a typical PBF process, the built component becomes surrounded by unfused powder particles as previously illustrated in Fig. 10a – b. However, the investigations in **Sections 4.1** to **4.3** failed to explore how these surrounding unfused powder particles might impact the efficacy of the *in-situ* ECM. In those cases, the EC sensor was positioned and used to scan only the as-built specimen surface during a scan pass.

In 2023, Sergeeva-Chollet et al., [137] addressed this issue, revealing that the presence of unfused powder surrounding the built component did not impact the signal-to-noise ratio during *in-situ* ECM assessments of AlSi7Mg samples. This was demonstrated by the significantly lower ECM signal magnitude in the unfused areas compared to the fused regions, as shown in Fig. 14a. Thus, despite the surrounding powder particles, *in-situ* ECM's ability to accurately identify engineered defects remained unaffected. In unpublished work by the authors, an XZ contour plot of the collected *in-situ* ECM signals also clearly distinguished the 316 L SS powder bed, the aluminium process chamber floor of the Aconity*MINI* PBF-LB machine, and ten 316 L SS samples fabricated with 10 different PBF-LB process parameters (Fig. 14b). The visualized data in Fig. 14b was captured using an AMiquam® *in-situ* ECM module, with an acquisition rate of 375 Hz, operating at an excitation frequency of 200 kHz, and an average lift-off of 690 μm.

4.5. *In-situ* GMR-based ECM for geometry characterization and subsurface feature detection

Detecting features beneath unfused metal powders poses significant challenges due to the shielding effect of the powder bed and limited

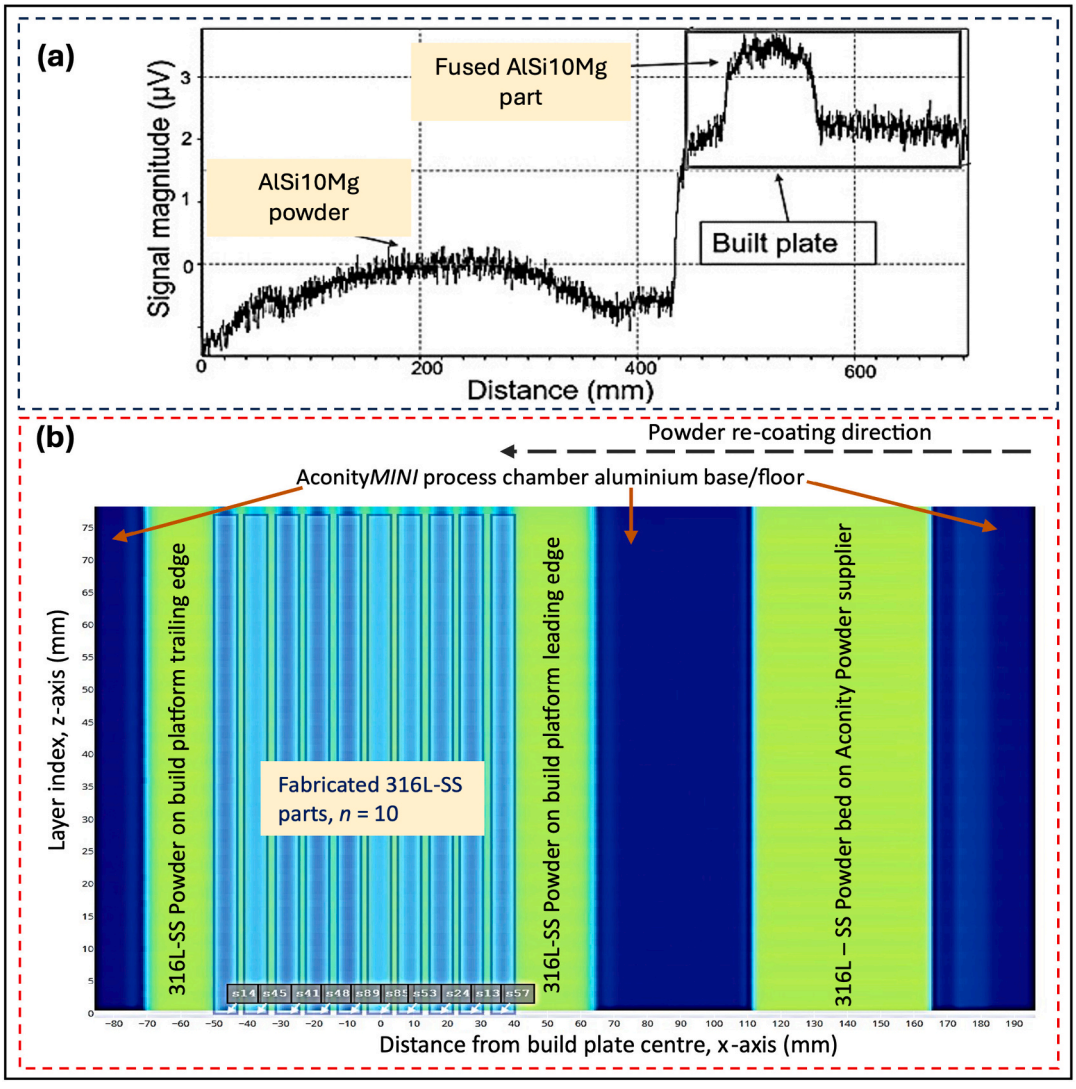


Fig. 14. (a) *In-situ* ECM signal magnitudes illustrating the contrast between a fused AlSi7Mg section and the surrounding unfused AlSi7Mg powder particles (adapted from Sergeeva-Chollet et al., [137]); (b) XZ view of an *in-situ* EC contour showing a clear distinction between a 316 L-SS powder bed and ten PBF-LB processed 316 L SS samples (Author's work).

penetration depths of traditional ECT methods (refer to **Section 2.8**), necessitating the advanced sensitivity and spatial resolution of MR-based ECT systems discussed in **Section 2.9,** Leveraging on these advanced capabilities of MR-based ECTs, Ehlers et al., [138] employed a giant magnetoresistive (GMR) sensor arrays for *in-situ* mapping of metal component being fabricated. The sensor array, integrated with the re-coater mechanism of an SLM280 HL PBF-LB machine, consisted of 128 MR elements with single-wire excitation and heterodyning. The study involved fabricating a 7.4 mm tall test sample of Haynes282 (a nickel-chromium-cobalt alloy) over 185 layers, each 40 μm thick. A primary excitation frequency (f_1) of 1 MHz and a bias voltage frequency (f_2) of 980 kHz produced a heterodyne frequency (f_3) of 20 kHz, allowing an estimated penetration depth of approximately 565 μm. To optimize measurement precision, the re-coater speed was reduced to 24 mm/s—one-tenth of its nominal speed—resulting in a tenfold increase in build time.

The *in-situ* GMR-based ECM successfully identified geometric features, including the contours of the topmost layer, sample edges from approximately ten preceding layers beneath unfused powder, and holes as deep as 1.12 mm. These results demonstrate the potential of GMR-based ECM for high-resolution geometry characterization and subsurface feature detection in PBF-LB processes, even in the presence of unfused metal powders.

5. Challenges and recommendations for *in-situ* ECM in metal AM

While Eddy Current Monitoring (ECM) has established itself as a reliable Non-Destructive Testing (NDT) method for *ex-situ* inspection of conventional components and shows promise in analysing volumetric discontinuities and relative density in metal Additive Manufacturing (AM) (as discussed in **Sections 3** and **4**), its broader application for both *ex-situ* assessment and *in-situ* monitoring of metal AM processes is constrained by several significant challenges. These challenges can be categorized into three key areas, as illustrated in the challenge pyramid (Fig. 15). The discussion below outlines these challenges in detail, accompanied by recommendations for overcoming them.

5.1. ECM module development and optimization

This category encompasses challenges related to the initial development, optimization, and implementation of the ECM module specifically tailored for *in-situ* monitoring in metal AM. These challenges include the need for advanced simulations, real-time processing capabilities, and the integration of machine learning and artificial intelligence to enhance ECM's performance and accuracy in real-time monitoring scenarios.

5.1.1. In-situ ECM module development for metal AM

A significant challenge in the advancement of *in-situ* ECM lies in the development of EC modules that can monitor the entire build platform during PBF-LB or PBF-ED processes. Currently, there is a scarcity of EC modules designed for *in-situ* ECM, and their adoption and integration by original equipment manufacturers (OEMs) remains limited. From the reviewed articles, the available OEM modules are coil-based EC probes whose effective sensing area within the monitored process plane is smaller than the overall build platform of the host AM machines. This means that only a few samples or the target samples carefully positioned within the EC scan path can be monitored for each build layer.

To emphasize this process plane width limitation based on the discussions in **Sections 3** and **4;** a key distinction between the pioneering *in-situ* ECM studies by Todorov et al., [119] and Ehlers et al., [138], and all other reviewed studies [47,113,134,136,139] lies in the type and configuration of the *in-situ* EC sensors. While Ehlers et al., [138] utilized a GMR-base EC-sensor array and Todorov et al., [119], used an array of 32 EC coil-based sensors, both had the advantage of a wider process plane width, enabling potential simultaneous monitoring of an entire build plate area in one scan pass. In contrast, the other studies utilized either a single or dual EC sensor configuration, resulting in significantly restricted process plane width. Therefore, the sample position on the build plate must align with the EC sensor path (refer to label item: Channel 1 (CH1) in **Fig. 12**), and the examined process plane area of the component must be within the effective testing width of the single or dual EC sensors as defined by the core diameter.

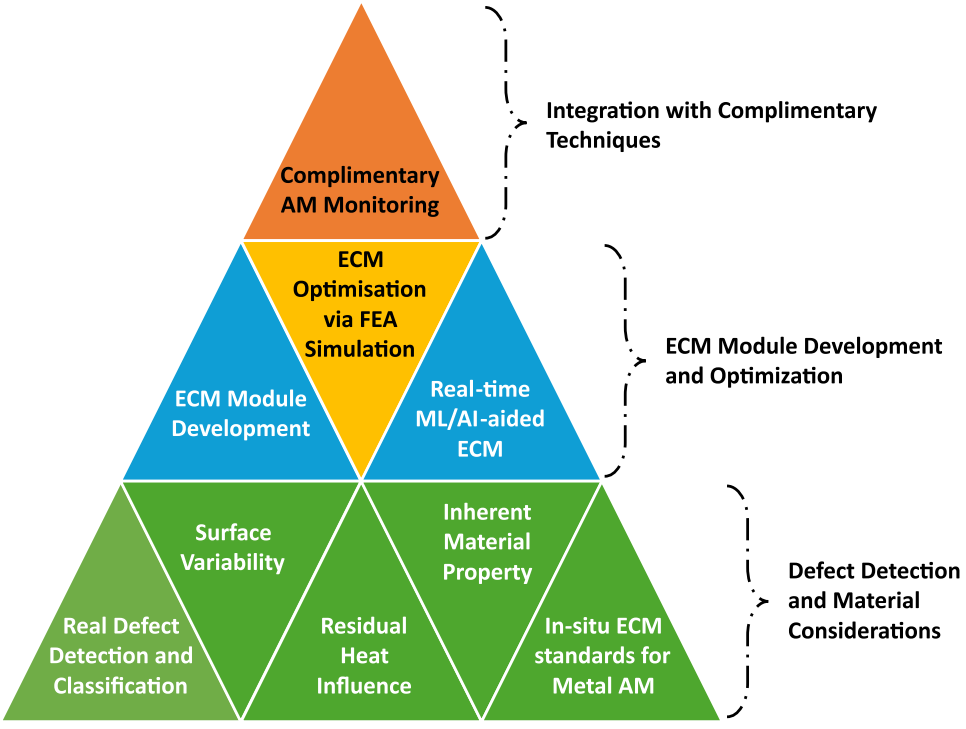


Fig. 15. *In-situ* eddy current monitoring challenge pyramid for metal AM monitoring.

This limitation emphasizes the imperative for continued innovation and advancement in ECM module technology to facilitate *in-situ* ECM of the entire build platform. Presently, the miniaturization potential of GMR-based EC sensors appears to hold greater promise compared to coil-based EC sensors (and EC sensor arrays).

5.1.2. EC parameter optimization in metal AM via FEA simulation

A cost-effective and efficient approach to determine the optimal lift-off EC parameter involves conducting an FE simulation study to analyze the air gap effect [43]. Additionally, other essential parameters for ECT can be estimated using Finite Element Analysis (FEA) software such as ANSYS Maxwell [66], COMSOL Multiphysics [140], or dedicated non-destructive evaluation (NDE) simulation tools like CIVA [141]. However, employing FEA simulation poses several challenges.

One major obstacle is the complexity of the electromagnetic fields and interactions between the probe and the test material [57,142,143]. FEA simulations demand a high level of expertise and computational resources, and their accuracy is heavily reliant on the selection of modelling parameters and assumptions. Moreover, the fidelity of the simulations can be compromised by the quality of the material property data, and the intricacies of the test specimen geometry due to edge effect and skin depth effect [112]. This complexity is exacerbated by the inability to accurately model the stochastic nature of the AM process (DED and PBF), and the resulting substantial disparities in material properties between conventionally manufactured and additively manufactured metallic components. In addition to accounting for residual heat effects in the FE models, these factors further complicate FE analysis and significantly curtail the effectiveness of *in-situ* ECM.

Another significant challenge is the necessity to validate FEA simulations against experimental data. This validation process is crucial for ensuring the accuracy and reliability of the simulations, as well as for identifying any limitations or assumptions that may impact the results. However, due to the relatively emerging nature of employing EC in metal AM, obtaining the requisite experimental data is not readily available.

5.1.3. Real-time in-situ ECM through machine learning and artificial intelligence

Real-time process control involves the continuous monitoring of process signals and part properties during the build, utilizing real-time data to provide feedback and enable dynamic adjustments to build parameters in a closed-loop manner [144]. Currently, *in-situ* ECM implementations are predominantly open-loop, meaning the collected data is post-processed offline to extract relevant information. The analysis results are then used to manually adjust the parameters for subsequent builds [145]. While functional, this approach is not resource-efficient and lacks responsiveness during the build process. To achieve near real-time *in-situ* ECM, it is crucial to study, optimize, and deploy algorithms powered by Machine Learning (ML) and Artificial Intelligence (AI). These algorithms would then be integrated into the software API architectures of metal AM OEMs to enable seamless feedback loops.

The incorporation of AI technologies into the *in-situ* EC system will enable automated flaw detection and characterization (size, shape, and defect position). An excellent example is the prediction of layer-by-layer porosity by Sallem et al., [135] from the EC-data. A well-trained convolutional neural network-based AI algorithm (CNN's) can identify patterns indicative of defects or anomalies while accounting for compositional changes (such as atomic Ni evaporation in NiTi) and variations in AM process chamber conditions that may influence the EC signals, such as increasing chamber temperature over longer build times, fluctuations in purging gas flow rate, and chamber pressure. Additionally, AI-based systems can adapt and learn from historical data, continuously improving the accuracy and efficiency of flaw detection and characterization over time.

By implementing real-time *in-situ* ECM through AI, quality control will be significantly improved, production downtime will be reduced, and the overall manufacturing process will be optimized. This recommendation underscores the importance of developing ML/AI algorithms and embracing advanced software architectures to harness the full potential of *in-situ* ECM for quality assurance in metal AM.

5.2. Defect detection and material considerations

This group addresses the complexities involved in accurately detecting and classifying defects, as well as the influence of material properties and process conditions. The inherent variability in surface conditions, the effects of residual heat, and the challenges posed by different material properties all contribute to the difficulties in ensuring reliable and accurate ECM during the AM process.

5.2.1. Real defect detection and classification

The magnetic field signal strength from defects is contingent upon the orientation of cracks relative to the flow direction of eddy currents within the sample [146]. Consequently, defects parallel to the surface may elude detection by ECT/ECM, particularly if they do not intersect with the eddy current. To mitigate sensitivity to defect orientation, an inducer capable of generating rotating magnetic flux density could be used. However, commercially available circular EC coil inducers struggle to achieve this rotating excitation type [146] which usually requires complex geometry excitation coils and production difficulties. Machado et al., [147] suggested the use of high magnetic permeability patterned substrates to shape the eddy currents distribution.

Moreover, the disparity between genuine (real) flaws and artificial defects adversely affects the interpretation of EC signals and the classification of defect types [107]. Current research efforts in both *ex-situ* ECT (**Section 3**) and *in-situ* ECM (**Section 4**) of AM components are predominantly concentrated on artificial defects characterized by predefined dimensions and defect areas (mm^2), significantly larger than those of real defects, such as pores and lack-of-fusion defects. Moreover, the orientation and position of artificial defects are not as randomized as real defects would be. These discrepancies pose a substantial challenge to the accuracy and adoption of *in-situ* ECM in metal AM, underscoring the necessity for further investigation into naturally occurring defects.

5.2.2. Surface variability and residual heat influence

Surface quality variability inherent to AM processes poses significant challenges for *in-situ* ECM [47]. Excessive surface roughness, often caused by balling due to suboptimal AM parameter selection, compromises ECM signal fidelity and complicates feature interpretation. Rough surfaces also introduce background noise into EC signals, reducing defect detection accuracy [46]. Uneven surfaces cause variations in lift-off—the critical distance between the probe and the material surface—which adversely impacts eddy current interactions with the material surface testing as discussed in **Section 2.5**. These variations create noise in the signal, potentially masking small near-surface defects. This challenge is particularly pronounced in SFEC methods using absolute and reflection EC probes, as shown in studies [60,66], but less so in MFEC techniques [84] (refer to Table 1).

Residual heat accumulation within the built AM part, as discussed in **Sections 2.4** and **3.3**, poses a significant challenge for *in-situ* ECM. Elevated surface temperatures can reduce ECT performance by approximately 30 % [69]. Suboptimal AM parameter selection often exacerbates this issue, leading to excessive heat buildup, uneven heating, and the development of thermal stresses within the component during fabrication. These stresses can result in layer delamination and warping, which increases the component height beyond the nominal value, interfering with the re-coater mechanism and causing scraping of the re-coater arm. During PBF processing of metallic powders with a high coefficient of thermal expansion (CTE) and low thermal conductivity, components are particularly susceptible to distortion and warping. Materials like AlSi10Mg, with a CTE of $\sim 20 \times 10^{-6}/°C$ at temperatures ranging from 25 to 100 °C [148], and excellent thermal

conductivity (120–160 W/m·K), have been the subject of limited investigations into temperature effects during *in-situ* ECM. The sole study to date, conducted by Spurek et al., [122], focused on AlSi10Mg (refer to **Section 4.2**).

However, other alloys with lower thermal conductivity, such as austenitic NiTi (CTE ~11×10^{-6}/°C) and martensitic NiTi (CTE ~6.6×10^{-6}/°C), remain unexplored in terms of their temperature effects on *in-situ* ECM performance. Investigating these materials could provide valuable insights into mitigating the impact of residual heat on EC signal fidelity.

To mitigate the impact of surface roughness and residual surface heat inherent in AM on the EC signal, and to minimize physical damage to the EC sensors, it may be necessary to move away from single-ECT whist introducing a suitable separation medium, such as Kapton film [43,118]. This medium can be directly applied to the tip of the EC probe as a replaceable consumable, tailored to the specific AM metal alloy being processed. However, further investigation into the effectiveness of this film, the exploration of alternative materials, and their effects on the SNR [93] is recommended for uncompromised and accurate EC measurements.

5.2.3. Inherent material property considerations

Adopting EC for *in-situ* metal AM monitoring also requires an understanding of the inherent material properties of the alloy powder and behaviour under electromagnetic interaction, which is also dependent on the set lift-off and EC frequency. However, the electrical and magnetic properties of the AM part are generally unknown. Therefore, the use of an EC calibration block of a different material and manufacturing technique will give inaccurate results [149].

For instance, Schneider et al., [59] conducted a comparison study and noted substantial differences between the eddy current conductivity (lift-off) curves at a 500 kHz testing frequency of a conventionally manufactured (cast) 17-4PH stainless steel standard conductivity specimen and a 17-4PH stainless steel specimen manufactured *via* PBF-LB. This indicates notable variations in material properties. Consequently, there is a need for further assessment of additional properties and quantitative analysis of conductivity differences, to investigate their impact on discontinuity detection signals during *in-situ* ECM.

From **Section 3** and Table 1, 316 L SS is a commonly studied AM metal alloy largely because it is cost-effective and widely available from numerous AM metal powder suppliers. However, among the various AM materials, NiTi presents notable challenges for *ex-situ/in-situ* eddy current testing and monitoring. This is mainly due to their high sensitivity to changes in chemical composition and temperature, as well as their susceptibility to thermally induced residual stresses during AM processing. In the case of PBF-LB technology, numerous studies, both analytical (utilizing numerical and FEA methods) and experimental, have confirmed the occurrence of preferential evaporation of nickel (Ni) [120,121,150–155]. This leads to significant alterations in the microstructural, mechanical, physical, shape memory, and superelastic properties of the alloy. The same can be said for PBF-EB processing of NiTi [156,157]. While there is yet no study specifically focusing on ECT/ECM assessments of neither conventionally manufactured nor AM-processed NiTi, it is clear that its electrical conductivity and magnetization properties would change as the composition changes, based on PBF processing conditions. The EC signals and interpretation may also be misleading, considering that residual heat temperatures may be much higher than the austenite finish (A_f) temperature of the newly melted NiTi layer. At temperatures $>A_f$ the crystal structure is cubic with nickel and titanium atoms positioned in a body-centred cubic (BCC) lattice. Conversely, a tetragonal or monoclinic crystal structure is observed at temperatures below martensite start M_s temperature, and a mixed and/or distorted cubic crystal structure at temperatures between M_f and A_f.

5.2.4. Lack of in-situ ECM standards for in-situ metal AM monitoring

The novelty and the recent research endeavours on *in-situ* ECM for metal AM underscores the need for developing measurement algorithms and software to streamline data acquisition and visualization of EC signals. This effort is crucial for laying the groundwork for ECM standards tailored to *in-situ* metal AM monitoring.

The absence of ECM standards in this emerging metal AM monitoring field presents a significant challenge, where precision and quality control of the produced metal components/parts are paramount. The standards aid in ensuring consistency and uniformity in ECM procedures across various AM systems and applications, thereby enhancing quality control throughout the metal AM workflow. Moreover, standardized ECM protocols will foster wider acceptance and adoption of ECM as a reliable *in-situ* monitoring tool within the metal AM industry.

Addressing this need for standardization is the focus of select research initiatives, such as the EU-funded Horizon Europe DILAPRO project (https://dilapro.eu/). The project aims to synergize *in-situ* ECM with high-speed infrared pyrometry, Finite Element Analysis (FEA), physical simulations, artificial intelligence (AI), and certification processes. Through endeavours like DILAPRO, there is potential for laying the foundation for *in-situ* monitoring standards.

5.3. Integration with complementary techniques

This area focuses on the challenges associated with integrating ECM with other monitoring and inspection techniques to provide a more comprehensive evaluation of AM components. The effective combination of ECM with other methods is crucial to overcoming the limitations of a single monitoring approach and enhancing the overall reliability and accuracy of *in-situ* assessments in metal AM.

5.3.1. ECT and complimentary monitoring techniques - Data fusion

No single testing method alone can fully assess the quality of metal AM parts *ex-situ*, just as no single *in-situ* monitoring technique can effectively track the AM build quality and monitor the AM build process. To tackle this issue, a promising strategy involves utilizing hyperspectral (multi-sensor) *in-situ* monitoring using complementary sensors such as acoustic emissions, ultrasonics, and infrared pyrometry, with ECM systems. This approach, known as data fusion, integrates various data sources and insights about the same physical object to create a cohesive, reliable, and precise representation [158,159]. By combining these diverse sources of information, the reliability and accuracy of the AM sensory system output are significantly enhanced. This is a leading direction in current *in-situ* metal AM monitoring research and funding initiatives. For example, similar to the objectives of the DILAPRO research project (https://dilapro.eu/), Phase3D® has been recently commissioned by the U.S. Air Force to develop a real-time inspection tool for additive manufacturing using multiple sensors (www.additivemonitoring.com).

However, the integration of multiple sensors presents its own set of challenges. These include the complexity of synchronizing different data streams, the potential for data overload, and the difficulty in calibrating and aligning sensor outputs to ensure consistent and accurate measurements. Without proper synchronization, the analysis may yield misleading results, as variations in timing can lead to inconsistencies in data interpretation. One potential solution is the adoption of event-driven data collection, where data collection is based on specific events or triggers rather than continuous streaming, helping to reduce the risk of synchronization errors.

Data overload is another challenge, as it can hinder decision-making processes and complicate the extraction of meaningful insights from the overwhelming volume of data generated by multiple sensors. This necessitates robust data management and analysis strategies to ensure that the most relevant and actionable information is highlighted.

Additionally, each sensor type may respond differently to variations in the AM process, making it difficult to create a unified interpretation of the data. Integrating AI techniques into EC data analysis, as demonstrated in previous studies [47,128,135,159,160], offers potential

solutions for real-time feature detection, classification, and overall enhancement of the monitoring process. Likewise, AI programs can also be used to interface with multiple sensor inputs and process them in parallel, ultimately contributing to the development of closed-loop digital twins of the AM process.

6. Conclusion

This review paper provides a comprehensive examination of the applicability of eddy current testing (ECT) for post-process assessment (*ex-situ* ECT) in metal AM, alongside a discussion of *in-situ* monitoring using EC technology (*in-situ* ECM), with exemplary case studies. By elucidating the fundamental principles of ECT and identifying the challenges and opportunities associated with its integration into metal AM processes, this review offers valuable insights into the evolving landscape of AM quality control. Key positive findings of the capabilities of ECT include:

- **Layer-by-layer density estimations:** *In-situ* ECT data allows for the reliable estimation of up layer-wise relative density of AlSi10M AM samples with up to 1000 layers with a mean absolute error of 0.126 %, using the temperature-compensated formula:

$$\rho_s(\sigma_r, T_s) = (0.0507 \times T_s) + (1.6024 \times \sigma_r) - 63.6758$$

- **Global Density Estimation: Applying the** temperature-compensated formula on *in-situ* ECT data, it is possible to estimate up to 99.95 ± 0.16 % global relative density of AlSi10M AM samples using the average layer-by-layer predicted relative density. Average prediction error $\Delta\rho_r$, compared to a μCT ground truth, is approximately 0.102.
- **Effect of Loose Powder:** Loose metal AM powder has a negligible effect on ECT accuracy.
- **Electrical Conductivity:** The electrical conductivity measured by ECT varies linearly with global relative density, with a strong correlation ($R^2 = 0.997$) in 316 L-SS metal components.
- ***In-situ* ECM with Sensor Arrays:** *In-situ* ECM using sensor arrays is generally ideal for AM monitoring, offering superior detection sensitivity and the ability to scan or cover a larger process plane.
- **Detection Capabilities:** ECT can detect artificial (engineered) surface-breaking defects as small as ~100 μm in width using coil-based ECMs.
- **Layer Resolution:** GMR EC arrays can fully resolve sample edges and geometry up to 164 layers (6.54 mm) from the build platform.
- *In-situ* ECM can be used to monitor **re-coater scraping**.

Despite these key positive findings and the broader promise of *in-situ* ECM for assessing process states and part qualities during AM builds, several considerations must be balanced, including real defect detection and defect resolution, cost, and integration challenges/requirements. Ongoing research is focused on addressing these concerns, with opportunities for developing EC sensors covering the entire build area and exploring multi-sensor integration strategies to overcome individual sensor limitations through *in-situ* hyperspectral monitoring. These challenges and recommendations underscore the importance of further research and development to address these limitations and fully exploit the potential of *in-situ* ECM in metal AM processing.

As this field progresses, we anticipate wider adoption of eddy current monitoring technologies and advancements towards closed-loop smart control systems or the development of AM digital twins. These innovations will facilitate the realization of intelligent and more sustainable metal additive manufacturing.

CRediT authorship contribution statement

Medad C.C. Monu: Writing – review & editing, Writing – original draft, Visualization, Methodology, Investigation, Formal analysis, Data curation, Conceptualization. **Josiah C. Chekotu:** Writing – review & editing, Formal analysis, Data curation. **Dermot Brabazon:** Writing – review & editing, Supervision, Resources, Project administration, Funding acquisition, Conceptualization.

Declaration of competing interest

The authors declare that they have no known competing financial interests or personal relationships that could have appeared to influence the work reported in this paper.

Acknowledgements

This publication has emanated from research supported by Science Foundation Ireland (SFI) under Grant Numbers 16/RC/3872, 21/RC/10295_P2 and is co-funded under the European Regional Development Fund, and from the European Union's Horizon Europe Research and Innovation Programme under grant agreement No. 101138859.

For Open Access, the authors have applied a CC BY public copyright license to any author accepted manuscript version arising from this submission.

References

[1] ISO/ASTM 52900–21. Additive manufacturing — General principles — Fundamentals and vocabulary. https://www.iso.org/standard/74514.html; 2021.
[2] Aboulkhair NT, Everitt NM, Ashcroft I, Tuck C. Reducing porosity in AlSi10Mg parts processed by selective laser melting. Addit Manuf 2014;1:77–86. https://doi.org/10.1016/j.addma.2014.08.001.
[3] Yadroitsev I. Selective laser melting: direct manufacturing of 3D-objects by selective laser melting of metal powders. Appl Catal B Environ 2009;75:229–38.
[4] Bourell D, Coholich J, Chalancon A, Bhat A. Evaluation of energy density measures and validation for powder bed fusion of polyamide. CIRP Ann - Manuf Technol 2017;66:217–20. https://doi.org/10.1016/j.cirp.2017.04.128.
[5] Marques BM, Andrade CM, Neto DM, Oliveira MC, Alves JL, Menezes LF. Numerical analysis of residual stresses in parts produced by selective laser melting process. Procedia Manuf 2020;47:1170–7. https://doi.org/10.1016/j.promfg.2020.04.167.
[6] Aconity3D GmbH©. Owner's Manual ACONITY MINI.. March 2019. Herzogenrath, Germany: Aconity3D GmbH; 2019.
[7] Vrancken B, Cain V, Knutsen R, Van Humbeeck J. Residual stress via the contour method in compact tension specimens produced via selective laser melting. Scr Mater 2014;87:29–32. https://doi.org/10.1016/j.scriptamat.2014.05.016.
[8] Thijs L, Montero Sistiaga ML, Wauthle R, Xie Q, Kruth JP, Van Humbeeck J. Strong morphological and crystallographic texture and resulting yield strength anisotropy in selective laser melted tantalum. Acta Mater 2013;61:4657–68. https://doi.org/10.1016/j.actamat.2013.04.036.
[9] Bowler N. Eddy-current nondestructive evaluation. Springer New York: New York, NY; 2019. https://doi.org/10.1007/978-1-4939-9629-2.
[10] Chen H, Xu Z, Zhou Z, Jin J, Hu Z. Study on the effect of Metal mesh on pulsed Eddy-current testing of corrosion under insulation using an early-phase signal feature. Materials (Basel) 2023;16:1451. https://doi.org/10.3390/ma16041451.
[11] Santos D, Machado MA, Monteiro J, Sousa JP, Proença CS, Crivellaro FS, et al. Non-destructive inspection of high temperature piping combining ultrasound and Eddy current testing. Sensors 2023;23:3348. https://doi.org/10.3390/s23063348.
[12] Taheri H, Jones C, Taheri M. Assessment and detection of stress corrosion cracking by advanced eddy current array nondestructive testing and material characterization. J Nat Gas Sci Eng 2022;102:104568. https://doi.org/10.1016/j.jngse.2022.104568.
[13] ASTM E3166–20. Guide for nondestructive examination of Metal additively manufactured aerospace parts after build. ASTM Int 2020:1–14. doi:https://doi.org/10.1520/E3166-20E01.
[14] ASTM_A450/A450M-21. Standard specification for general requirements for carbon, ferritic alloy, and austenitic alloy steel tubes. West Conshohocken, PA: ASTM International; 2021.
[15] ASTM_B244-15. Standard test method for measurement of thickness of anodic coatings of aluminum and other nonconductive coatings on Nonmagnetic Base materials with Eddy-current instruments. West Conshohocken, PA: ASTM International; 2015.

[16] ASTM_E690-20. Standard practice for in-situ electromagnetic (Eddy-current) examination of nonmagnetic heat exchanger tubes. West Conshohocken, PA: ASTM International; 2020.
[17] ASTM_E703-21. Standard practice for electromagnetic (eddy current) sorting of nonferrous metals. West Conshohocken, PA: ASTM International; 2021.
[18] ASTM_E1004-21. Standard practice for electromagnetic (eddy current) measurements of electrical conductivity. West Conshohocken, PA: ASTM International; 2021.
[19] ASTM_E1033-21. Standard practice for electromagnetic (eddy current) examination of type F continuously welded (CW) ferromagnetic pipe and tubing above the curie temperature. West Conshohocken, PA: ASTM International; 2021.
[20] ASTM_E1316-21. Standard terminology for nondestructive examinations. West Conshohocken, PA: ASTM International; 2021.
[21] ASTM_G46-21. Standard guide for examination and evaluation of pitting corrosion. West Conshohocken, PA: ASTM Int. ASTM International; 2021.
[22] ASTM_E2934–14. Standard practice for calibration of eddy current testing instruments. West Conshohocken, PA: ASTM International; 2018.
[23] ASTM_E3052–16. Standard Test Method for Detection and Characterization of Surface and Subsurface Cracks in Dissimilar Metal Welds by Eddy Current Testing 2016.
[24] ASTM_E2884–17. Standard practice for in-service inspection of heat exchanger tubes using eddy current testing. West Conshohocken, PA: ASTM International; 2017.
[25] ASTM_E309-16. Standard test method for magnetic particle testing. West Conshohocken, PA: ASTM International; 2016.
[26] ASTM_B659-17. Standard guide for measurement of thickness of metallic coatings on nonmetallic substrates. West Conshohocken, PA: ASTM International; 2017.
[27] STP1151. Standard Test Methods for Nondestructive Examination of Aerospace Materials n.d.
[28] ASTM_E690-15_2020. Standard practice for conducting an interlaboratory study to determine the precision of a test method. West Conshohocken, PA: ASTM International; 2020.
[29] ASTM_E566–19. Standard guide for evaluating the capability of a nondestructive testing method. West Conshohocken, PA: ASTM International; 2019.
[30] ASTM_E703–20. Standard practice for calibration of magnetic particle testing equipment. West Conshohocken, PA: ASTM International; 2020.
[31] ASTM_E215-19. Standard method for standardizing equipment for electromagnetic testing of seamless aluminum-alloy tube. West Conshohocken, PA: ASTM International; 2019.
[32] ASTM_E243-21. Standard practice for electromagnetic (eddy-current) testing of seamless copper and copper-alloy tubes. West Conshohocken, PA: ASTM International; 2021.
[33] ASTM_E309-21. Standard practice for eddy current examination of steel tubular products using magnetic saturation. West Conshohocken, PA: ASTM International; 2021.
[34] ASTM_E376-21. Standard practice for measuring coating thickness by magnetic-field or eddy-current (electromagnetic) test methods. West Conshohocken, PA: ASTM International; 2021.
[35] ASTM_E426-21. Standard practice for electromagnetic (eddy current) testing of seamless and welded tubular products, austenitic stainless steel and similar alloys. West Conshohocken, PA: ASTM International; 2021.
[36] ASTM_E566-21. Standard practice for electromagnetic (eddy current) sorting of ferrous metals. West Conshohocken, PA: ASTM International; 2021.
[37] ASTM_E571-21. Standard practice for electromagnetic (eddy-current) examination of nickel and nickel alloy tubular products. West Conshohocken, PA: ASTM International; 2021.
[38] Bruchwald O, Frackowiak W, Zwoch S, Reimche W, Maier HJ. In-Situ Monitoring of the Microstructure Evolution Using Eddy Current Technology 2016:1–7.
[39] Uchanin V, Minakov S, Nardoni G, Ostash O, Bentoglio M. Eddy current method for evaluation of stresses in steel components. 14th Int Conf Slov Soc Non-Destructive Test &Quot;Application Contemp Non-Destructive Test Eng Conf Proc 2017; 2017-Septe: 207–12.
[40] Botko F, Zajac J, Czan A, Radchenko S, Lehocka D, Duplak J. Influence of residual stress induced in steel material on Eddy currents response parameters. In: Gapiński B, Szostak M, Ivanov V, editors. Adv. Manuf. II. Cham: Springer International Publishing; 2019. p. 551–60. https://doi.org/10.1007/978-3-030-16943-5_47.
[41] Chen Z, Jomdecha C, Xie S. Eddy Current Testing. In: Ida N, Meyendorf N, editors. Handb. Adv. Nondestruct. Eval., Cham: Springer International Publishing; 2019, p. 645–728. https://doi.org/10.1007/978-3-319-26553-7_40.
[42] García-Martín J, Gómez-Gil J, Vázquez-Sánchez E. Non-destructive techniques based on Eddy current testing. Sensors 2011;11:2525–65. https://doi.org/10.3390/s110302525.
[43] Saddoud R, Sergeeva-Chollet N, Darmon M. Eddy current sensors optimization for defect detection in parts fabricated by laser powder bed fusion. Sensors 2023;23:4336. https://doi.org/10.3390/s23094336.
[44] Kemerling B, Ryan D. Development of Production Eddy Current Inspection Process for Additively Manufactured Industrial Gas Turbine Engine Components. Vol. 6 Ceram. Control. Diagnostics, Instrumentation; Educ. Manuf. Mater. Metall., vol. 6, American Society of Mechanical Engineers; 2019, p. 1–8. https://doi.org/10.1115/GT2019-90971.
[45] Kalliopi K, Aligizaki D. Nondestructive testing overview, volume 10 of the nondestructive testing handbook. Anti-Corrosion Methods Mater 2003;50. https://doi.org/10.1108/acmm.2003.12850dae.001.
[46] Du W, Bai Q, Wang Y, Zhang B. Eddy current detection of subsurface defects for additive/subtractive hybrid manufacturing. Int J Adv Manuf Technol 2018;95:3185–95. https://doi.org/10.1007/s00170-017-1354-2.
[47] Spurek MA, Spierings AB, Lany M, Revaz B, Santi G, Wicht J, et al. In-situ monitoring of powder bed fusion of metals using eddy current testing. Addit Manuf 2022;60:103259. https://doi.org/10.1016/j.addma.2022.103259.
[48] Geľatko M, Hatala M, Botko F, Vandžura R, Hajnyš J. Eddy current testing of artificial defects in 316L stainless steel samples made by additive manufacturing technology. Materials (Basel) 2022;15:6783. https://doi.org/10.3390/ma15196783.
[49] Ye C, Laureti S, Malekmohammadi H, Wang Y, Ricci M. Swept-frequency eddy current excitation for TMR array sensor and pulse-compression: feasibility study and quantitative comparison of time and frequency domains processing. Measurement 2022;187:110249. https://doi.org/10.1016/j.measurement.2021.110249.
[50] Sophian A, Tian G, Fan M. Pulsed Eddy current non-destructive testing and evaluation: A review. Chin J Mech Eng 2017;30:500–14. https://doi.org/10.1007/s10033-017-0122-4.
[51] NDT Supply. Eddy current inspection method. Nondestruct Insp Methods, Basic Theory 2016:4.1–4.118. https://content.ndtsupply.com/media/EddyCurrent-USAF-Tech-Manual-N-R.pdf. [Accessed 3 May 2024].
[52] ASSDA. Australian Stainless Steel Development Association Magnetic Effects of Stainless Steels. ASSDA Tech FAQ No 3 n.d.:3–4. https://doi.org/https://www.assda.asn.au/images/PDFs/FAQs/FAQ3.pdf.
[53] Lyamkin V, Boller C. Magnetic methods for evaluation of bcc and bct iron fractions below 0.1% in austenite: surface mapping and full volume evaluation. 26th Int Conf Struct Mech React Technol 2022.
[54] Sukhon R, Kongchana R, Khongsiri K, Puntaratronnugoon B, Tulasombut V. A study on volumetric magnetic susceptibility of weight due to its manufacturing process. 21st Conf Meas Force, Mass Torque Together with HARDMEKO 2010 2nd Meet Vib Meas IMEKO TC3, TC5 TC22 Conf 2010:303–6.
[55] Strecker Z, Kubík M, Vítek P, Roupec J, Paloušek D, Šreibr V. Structured magnetic circuit for magnetorheological damper made by selective laser melting technology. Smart Mater Struct 2019;28:055016. https://doi.org/10.1088/1361-665X/ab0b8e.
[56] Fofanov D, Riedner S. Magnetic properties of stainless steels: Applications, opportunities and new developments. In: Proc. 2011 world Stainl. Steel Conf. vol. 29. Expo, Maastricht, Netherlands; 2011.
[57] AbdAlla AN, Faraj MA, Samsuri F, Rifai D, Ali K, Al-Douri Y. Challenges in improving the performance of eddy current testing: review. Meas Control 2019;52:46–64. https://doi.org/10.1177/0020294018801382.
[58] TWI Global. What factors affect Eddy currents? Tech Knowl. https://www.twi-global.com/technical-knowledge/faqs/faq-what-factors-affect-eddy-currents. [Accessed 24 November 2024].
[59] Schneider B, Shoaib MRBM, Taheri H, Koester L, Bigelow T, Bond LJ. Nondestructive evaluation of additively manufactured Metal components with an Eddy current technique. ASNT 27th Annu. Res Symp Proc, ASNT 2018:182–90. https://doi.org/10.32548/RS.2018.019.
[60] Guo S, Ren G, Zhang B. Subsurface defect evaluation of selective-laser-melted Inconel 738LC alloy using Eddy current testing for additive/subtractive hybrid manufacturing. Chinese J Mech Eng English Ed 2021:34. https://doi.org/10.1186/s10033-021-00633-9.
[61] Lim HJ, Lee J, Sohn H. Eddy-current lift-off effect compensation for 3-D printed Ti-6Al-4V components with various electrical conductivities. IEEE Trans Instrum Meas 2023;72:1–8. https://doi.org/10.1109/TIM.2023.3295460.
[62] Sheikh Amiri M, Kashefi M. Investigation of variables affecting impedance plane in Eddy current testing of carburized steels. J Mater Eng Perform 2011;20:476–80. https://doi.org/10.1007/s11665-010-9697-y.
[63] Hippert DF. High resolution eddy current inspection and eddy current testing for additive manufacturing. EPFL 2016. https://doi.org/10.5075/epfl-thesis-6746.
[64] Bell RJ, Birks AS. An Engineer's Guide to Eddy Current Testing. Vol. 1 Fuels Combust. Mater. Handl. Emiss. Steam Gener. Heat Exch. Cool. Syst. Turbines, Gener. Aux. Plant Oper. Maint., vol. 1, American Society of Mechanical Engineers; 2013, p. 1–8. https://doi.org/10.1115/POWER2013-98297.
[65] NDE-ED.org. Mode of Operation. Nondestruct Eval Tech Eddy Curr Test 2023. https://www.nde-ed.org/NDETechniques/EddyCurrent/Instrumentation/analogmeter.xhtml (accessed April 24, 2024).
[66] E. Farag H, Toyserkani E, Khamesee MB.. Non-destructive testing using Eddy current sensors for defect detection in additively manufactured titanium and stainless-steel parts. Sensors 2022;22:5440. https://doi.org/10.3390/s22145440.
[67] Knörzer H. Fundamentals of eddy current testing. https://collab.dvb.bayern/display/TUMzfp/Fundamentals+of+eddy+current+testing. [Accessed 15 January 2024].
[68] Nikkoshi Co. Ltd. MR Sensor Technology. MR Sens Tech Inf 2024. https://www.nikkoshi.co.jp/english/technology/mrsensor.html (accessed October 25, 2024).
[69] Ehlers H, Pelkner M, Thewes R. Heterodyne Eddy current testing using Magnetoresistive sensors for additive manufacturing purposes. IEEE Sensors J 2020;20:5793–800. https://doi.org/10.1109/JSEN.2020.2973547.
[70] Elzwawy A, Rasly M, Morsy M, Piskin H, Volmer M. Magnetic Sensors: Principles, Methodologies, and Applications. In: Ali GAM, Chong KF, Makhlouf ASH, editors. Handb. Nanosensors, Cham: Springer Nature Switzerland; 2024, p. 1–38. https://doi.org/10.1007/978-3-031-16338-8_33-1.
[71] Rifai D, Abdalla A, Ali K, Razali R. Giant Magnetoresistance sensors: A review on structures and non-destructive Eddy current testing applications. Sensors 2016;16:298. https://doi.org/10.3390/s16030298.

[72] Ghoni R, Dollah M, Sulaiman A, Mamat Ibrahim F. Defect characterization based on Eddy current technique: technical review. Adv Mech Eng 2014;2014. https://doi.org/https://doi.org/10.1155/2014/182496.

[73] Sophian A, Tian GY, Taylor D, Rudlin J. Electromagnetic and eddy current NDT: A review. Insight Non-Destructive Test Cond Monit 2001;43:302–6.

[74] Peng X, Kong L, An H, Dong G. A review of in situ defect detection and monitoring technologies in selective laser melting. 3Dvol. 10. Print Addit Manuf; 2023. p. 438–66. https://doi.org/10.1089/3dp.2021.0114.

[75] Chauveau D. Review of NDT and process monitoring techniques usable to produce high-quality parts by welding or additive manufacturing. Weld World 2018;62:1097–118. https://doi.org/10.1007/s40194-018-0609-3.

[76] Segovia Ramírez I, García Márquez FP, Papaelias M. Review on additive manufacturing and non-destructive testing. J Manuf Syst 2023;66:260–86. https://doi.org/10.1016/j.jmsy.2022.12.005.

[77] Mandache C. Overview of non-destructive evaluation techniques for metal-based additive manufacturing. Mater Sci Technol 2019;35:1007–15. https://doi.org/10.1080/02670836.2019.1596370.

[78] NDE-ED.org (web archive link, 22 April 2024). Advanced Eddy Current Techniques Background. Nondestruct Eval Tech Eddy Curr Test n.d.:4. https://www.nde-ed.org/NDETechniques/EddyCurrent/AdvancedTechniques/background.xhtml (accessed April 22, 2024).

[79] Fernandez NM, Charlton PC, Granville RK. Pulsed Eddy current CUI simulation with coupled electric circuit analysis using Quickfield FEA. E-Journal Nondestruct Test 2019:1–10.

[80] Belkacem G, Loete F, Phulpin T. Broadband Eddy current measurement of the sheet resistance of GaN semiconductors. Sensors 2024;24:1–8. https://doi.org/10.3390/s24051629.

[81] Lu M, Xie Y, Zhu W, Peyton A, Yin W. Determination of the magnetic permeability, electrical conductivity, and thickness of ferrite metallic plates using a multifrequency electromagnetic sensing system. IEEE Trans Ind Informatics 2019;15:4111–9. https://doi.org/10.1109/TII.2018.2885406.

[82] Zhou Z, Qin M, Xie Y, Tan J, Bao H. Experimental study of microstructures in Bias weld of coiled tubing steel strip with multi-frequency Eddy current testing. IEEE Access 2020;8:48241–51. https://doi.org/10.1109/ACCESS.2020.2979414.

[83] Bobrov I, Epp J. Microscaled multi-frequency Eddy current analysis for high throughput characterization of steel Micro-samples. J Nondestruct Eval 2023;42:1–13. https://doi.org/10.1007/s10921-023-00930-4.

[84] Obaton A-FF, Lê M-Q, Prezza V, Marlot D, Delvart P, Huskic A, et al. Investigation of new volumetric non-destructive techniques to characterise additive manufacturing parts. Weld. World 2018;62:1049–57. https://doi.org/10.1007/s40194-018-0593-7.

[85] Janousek L, Stubendekova A, Smetana M. Novel insight into swept frequency eddy-current non-destructive evaluation of material defects. Measurement 2018;116:246–50. https://doi.org/10.1016/j.measurement.2017.11.039.

[86] Smetana M, Gombarska D, Psenakova Z. Progress in evaluation of deep artificial defects from sweep-frequency Eddy-current testing signals. Sensors 2023:23. https://doi.org/10.3390/s23136085.

[87] Zhao F, Chen D, Pu Z, Wang J. A new research method for corrosion defect in metal pipeline by using pulsed Edd y current. Am Soc Mech Eng Press Vessel Pip Div PVP 2020;7:1–7. https://doi.org/10.1115/PVP2020-21322.

[88] Fang Y, Qu Y, Zeng X, Chen H, Xie S, Wan Q, et al. Distinguishing evaluation of plastic deformation and fatigue damage using pulsed eddy current testing. NDT E Int 2023;140:102972. https://doi.org/10.1016/j.ndteint.2023.102972.

[89] Huang S, Wang S. The pulsed Eddy current testing. In: New Technol. Electromagn. Non-destructive test. Singapore: Springer Singapore; 2016. p. 41–80. https://doi.org/10.1007/978-981-10-0578-7_2.

[90] Franco F, Cardoso FA, Rosado LS, Ferreira R, Cardoso S, Piedade M, et al. Advanced NDT inspection tools for titanium surfaces based on high-performance Magnetoresistive sensors. IEEE Trans Magn 2017:53. https://doi.org/10.1109/TMAG.2016.2636807.

[91] Rutronik. Magnetometers - Exciting possibilities with TMR technology 2019;11:1–14. https://www.rutronik.com/article/magnetometers-exciting-possibilities-with-tmr-technology#:~:text=1).,ferromagnetic layer to the other. (accessed November 25, 2024).

[92] Pelkner M, Pohl R, Erthner T, Stegemann R, Kreutzbruck M, Sergeeva-Chollet N, et al. Eddy Current Testing With High-Spatial Resolution Probes Using Mr Arrays As Receiver. 7th Int Symp NDT Aerosp 2015:2011–4.

[93] Caetano DM, Rabuske T, Fernandes J, Pelkner M, Fermon C, Cardoso S, et al. High-resolution nondestructive test probes based on Magnetoresistive sensors. IEEE Trans Ind Electron 2019;66:7326–37. https://doi.org/10.1109/TIE.2018.2879306.

[94] Smith CH. Eddy-Current Testing with GMR Magnetic Sensor Arrays. AIP Conf. Proc., vol. 700, AIP; 2004, p. 406–13. doi:https://doi.org/10.1063/1.1711651.

[95] Berkache A, Lee J, Choe E. Evaluation of cracks on the welding of austenitic stainless steel using experimental and numerical techniques. Appl Sci 2021;11:1–12. https://doi.org/10.3390/app11052182.

[96] Berkache A, Lee J, Wang D, Park D-G. Development of an Eddy current test configuration for welded carbon steel pipes under the change in physical properties. Appl Sci 2021;12:93. https://doi.org/10.3390/app12010093.

[97] Bui L-V, Jeng J-T, Huang H-C, Nguyen H-T, Doan V-D, Nguyen T-H, et al. High-resolution flaw detection using Eddy current probe Array based on Giant Magnetoresistance sensors. IEEE Trans Magn 2024;60:1–5. https://doi.org/10.1109/TMAG.2024.3402331.

[98] Nguyen HT, Jeng JT, Doan VD, Dinh CH, Dao DV, Pham TT, et al. Surface and subsurface Eddy-current imaging with GMR sensor. IEEE Trans Instrum Meas 2021;70:1–10. https://doi.org/10.1109/TIM.2021.3120378.

[99] Bailey J, Long N, Hunze A. Eddy current testing with Giant Magnetoresistance (GMR) sensors and a pipe-encircling excitation for evaluation of corrosion under insulation. Sensors 2017;17:2229. https://doi.org/10.3390/s17102229.

[100] Romero-Arismendi NO, Pérez-Benítez JA, Ramírez-Pacheco E, Espina-Hernández JH. Design method for a GMR-based eddy current sensor with optimal sensitivity. Sensors Actuators A Phys 2020;314:112348. https://doi.org/10.1016/j.sna.2020.112348.

[101] Vacher F, Alves F, Gilles-Pascaud C. Eddy current nondestructive testing with giant magneto-impedance sensor. NDT E Int 2007;40:439–42. https://doi.org/10.1016/j.ndteint.2007.02.002.

[102] Falque R, Vidal-Calleja T, Miro JV. Defect detection and segmentation framework for remote field Eddy current sensor data. Sensors (Basel) 2017:17. https://doi.org/10.3390/s17102276.

[103] Zhang W, Shi Y, Li Y, Luo Q. A study of quantifying thickness of ferromagnetic pipes based on remote field Eddy current testing. Sensors (Basel) 2018:18. https://doi.org/10.3390/s18092769.

[104] Zhang L, Deng R, Ning N, Fan J, Wang W, Song K. Study on remote field Eddy current testing Technology for Crack-like Defects in Long truss structure of aircraft. Mater (Basel, Switzerland); 2022. p. 15. https://doi.org/10.3390/ma15155093.

[105] Ma YP, Wikswo JP. SQUID Magnetometers for Depth-Selective, Oriented Eddy Current Imaging. In: Thompson DO, Chimenti DE, editors. Rev. Prog. Quant. Nondestruct. Eval. Vol. 17A, Boston, MA: Springer US; 1998, p. 1067–74. doi:https://doi.org/10.1007/978-1-4615-5339-7_138.

[106] Vettoliere A, Granata C. Highly sensitive tunable magnetometer based on superconducting quantum interference device. Sensors 2023:23. https://doi.org/10.3390/s23073558.

[107] Yusa N, Chen W, Hashizume H. The Application of 3D Printing Technology to Fabricate an Imitative Crack for Electromagnetic NDT&E Studies. In: Ramos HG, Ribeiro AL, editors. Electromagn. Nondestruct. Eval., IOS Pres; 2017, p. 150–6. doi:https://doi.org/10.3233/978-1-61499-767-2-150.

[108] Kobayashi N, Yamamoto S, Sugawara A, Nakane M, Tsuji D, Hino T, et al. Fundamental experiments of eddy current testing for additive manufacturing metallic material toward in-process inspection. 45th Annu. Rev. Prog. Quant. Nondestruct. Eval., vol. 38, AIP Publishing; 2019, p. 070003–1 to 070003–7. doi:https://doi.org/10.1063/1.5099803.

[109] D'Accardi E, Krankenhagen R, Ulbricht A, Pelkner M, Pohl R, Palumbo D, et al. Capability to detect and localize typical defects of laser powder bed fusion (L-PBF) process: an experimental investigation with different non-destructive techniques. Prog Addit Manuf 2022;7:1239–56. https://doi.org/10.1007/s40964-022-00297-4.

[110] Hippert D, Jhabvala J, Boillat E, Santi G, Bleuler H. Development of an Eddy current testing method as process control for additive manufacturing of metallic components. 2015 IFToMM world Congr proceedings, IFToMM 2015 2015:10–4. doi:https://doi.org/10.6567/IFToMM.14TH.WC.OS20.022.

[111] Spurek MA, Luong VH, Spierings AB, Lany M, Santi G, Revaz B, et al. Relative density measurement of PBF-manufactured 316L and AlSi10Mg samples via Eddy current testing. Metals (Basel) 2021;11:1376. https://doi.org/10.3390/met11091376.

[112] Kasa T, Sun W, Hatsukade Y, Yonehara M, Ikeshoji T-T, Kyogoku H. Eddy current testing based non-destructive inspection for Metal 3D additive manufacturing objects with HTS-SQUID. IEEE Trans Appl Supercond 2023;33:1–4. https://doi.org/10.1109/TASC.2023.3248001.

[113] Spierings AB, Spurek MA, Lany M, Santi G, Revaz B, Wegener K. Direct part density inspection in laser powder bed fusion using eddy current testing. Euspen's Spec Interes Gr Meet Adv Precis Addit Manuf 2021. https://doi.org/10.3929/ethz-b-000516133.

[114] Gruber S, Stepien L, López E, Brueckner F, Leyens C. Physical and geometrical properties of additively manufactured pure copper samples using a green laser source. Materials (Basel) 2021;14:3642. https://doi.org/10.3390/ma14133642.

[115] Barrancos A, Batalha RL, Rosado LS. Towards enhanced Eddy current testing Array probes scalability for powder bed fusion layer-wise imaging. Sensors 2023;23:2711. https://doi.org/10.3390/s23052711.

[116] Eisenbarth D, Stoll P, Klahn C, Heinis TB, Meboldt M, Wegener K. Unique coding for authentication and anti-counterfeiting by controlled and random process variation in L-PBF and L-DED. Addit Manuf 2020;35:101298. https://doi.org/10.1016/j.addma.2020.101298.

[117] Yusa N, Chen W, Wang J, Hashizume H. Fabrication of imitative cracks by 3D printing for electromagnetic nondestructive testing and evaluations. Case Stud Nondestruct Test Eval 2016;5:9–14. https://doi.org/10.1016/j.csndt.2016.03.004.

[118] Bento JB, Lopez A, Pires I, Quintino L, Santos TG. Non-destructive testing for wire + arc additive manufacturing of aluminium parts. Addit Manuf 2019;29:100782. https://doi.org/10.1016/j.addma.2019.100782.

[119] Todorov EI, Boulware P, Gaah K. Demonstration of array eddy current technology for real-time monitoring of laser powder bed fusion additive manufacturing process. In: Shull PJ, editor. Nondestruct. Charact. Monit. Adv. Mater. Aerospace, Civ. Infrastructure, Transp. XII, SPIE; 2018, p. 40. doi:https://doi.org/10.1117/12.2297511.

[120] Monu MCC, Ekoi EJ, Hughes C, Kumar SS, Brabazon D. Resultant physical properties of as-built nitinol processed at specific volumetric energy densities and correlation with in-situ melt pool temperatures. J Mater Res Technol 2022;21:2757–77. https://doi.org/10.1016/j.jmrt.2022.10.073.

[121] Obeidi MA, Monu MCC, Hughes C, Bourke D, Dogu MN, Francis J, et al. Laser beam powder bed fusion of nitinol shape memory alloy (SMA). J Mater Res Technol 2021;14:2554–70. https://doi.org/10.1016/j.jmrt.2021.07.126.

[122] Spurek MA, Spierings AB, Lany M, Revaz B, Santi G, Wicht J, et al. Influence of part temperature on in-situ monitoring of powder bed fusion of metals using eddy current testing. Prog Addit Manuf 2024;V. https://doi.org/10.1007/s40964-024-00600-5.
[123] Mukherjee S, Benavidez E, Tringe JW, Peng L, Deng Y, Stobbe D. An In-Situ Eddy Current Diagnostic for Temperature Monitoring in Metal Additive Manufacturing. IEEE Antennas Propag Soc AP-S Int Symp 2023; 2023-July: 341–2. doi:https://doi.org/10.1109/USNC-URSI52151.2023.10237400.
[124] Dogaru· T, Smith ST. EDGE CRACK DETECTION USING A GIANT MAGNETORESISTANCE BASED EDDY CURRENT SENSOR. Nondestruct Test Eval 2000; 16:31–53. doi:https://doi.org/10.1080/10587750008953062.
[125] Haddad A, Zergoug M, Azzaz M, Tafat A, Bergheul S. Monitoring of metal powder by eddy current. Int J Microstruct Mater Prop 2010;5:3. https://doi.org/10.1504/IJMMP.2010.032497.
[126] Bahramyan M, Mousavian RT, Perumal G, Griffin GR, Rohmat Aji Pradana Y, Carton JG, et al. Design of novel high entropy alloys based on the end-of-life recycling rate and element lifetime for cryogenic applications. Mater Des 2024; 246:113316. https://doi.org/10.1016/j.matdes.2024.113316.
[127] Miracle DB. High entropy alloys as a bold step forward in alloy development. Nat Commun 2019;10:1–3. https://doi.org/10.1038/s41467-019-09700-1.
[128] Tomizawa T, Yusa N. Bayesian data fusion of eddy current testing for flaw characterization with uncertainty evaluation. NDT E Int 2024;141:102996. https://doi.org/10.1016/j.ndteint.2023.102996.
[129] Ida N, Betzold K, Lord W. Finite element modeling of absolute eddy current probe signals. J Nondestruct Eval 1982;3:147–54. https://doi.org/10.1007/BF00566556.
[130] Bakhtiari S, Kupperman DS. Modeling of eddy current probe response for steam generator tubes. Nucl Eng Des 1999;194: 57–71. https://doi.org/10.1016/S0029-5493(99)00169-7.
[131] Lakhdari AE, Cheriet A, El-Ghoul IN. Skin effect based technique in eddy current non-destructive testing for thickness measurement of conductive material. IET Sci Meas Technol 2019;13:255–9. https://doi.org/10.1049/iet-smt.2018.5322.
[132] Stucky P, Lord W. Skin Depth Considerations in Eddy Current NDT. In: Thompson DO, Chimenti DE, editors. Rev. Prog. Quant. Nondestruct. Eval., Boston, MA: Springer US; 1992, p. 299–306. doi:https://doi.org/10.1007/978-1-4615-3344-3_37.
[133] Metal AM. Mission possible: the five year plan to gain FAA and EASA acceptance of in-process monitoring. Inovar Commun 2023:9. https://issuu.com/inovar-communications/docs/metal_am_winter_2023_issuu/146 [accessed February 2, 2024].
[134] Zimermann R, Mohseni E, Foster EA, Vasilev M, Loukas C, Vithanage RKW, et al. In-process non-destructive evaluation of metal additive manufactured components at build using ultrasound and eddy-current approaches. J Manuf Process 2023;107:549–58. https://doi.org/10.1016/j.jmapro.2023.10.063.
[135] Sallem H, Ghorbel H, Goffinet E, Cinna A, Pralong J, Wicht J, et al. In-situ monitoring of selective laser melted Ti–6Al–4V parts using Eddy current testing and machine learning. In: T. M, H. S, F. G, H. S, N. B, editors. Lect. Notes Mech. Eng., Springer Science and Business Media Deutschland GmbH; 2024, p. 139–48. doi:https://doi.org/10.1007/978-3-031-47784-3_18.
[136] Peng L, Deng Y, Benavidez E, Mukherjee S, Morales RE, Tringe J, et al. In-situ 3D Temperature Field Modeling and Characterization using Eddy Current for Metal Additive Manufacturing Process Monitoring. ASNT Res. Symp. 2023 Proc., The American Society for Nondestructive Testing Inc.; 2023, p. 24. 10.32548/RS.2023.039.
[137] Sergeeva-Chollet N, Perlin K, Pellat M. Development of instrumentation for eddy current in situ monitoring of laser powder bed fusion. Weld World 2023;67: 1105–12. https://doi.org/10.1007/s40194-022-01456-5.
[138] Ehlers H, Pelkner M, Thewes R. Online process monitoring for additive manufacturing using Eddy current testing with Magnetoresistive sensor arrays. IEEE Sensors J 2022;22:19293–300. https://doi.org/10.1109/JSEN.2022.3205177.
[139] Sallem H, Ghorbel H, Goffinet E, Cinna A, Pralong J, Wicht J, et al. In-situ monitoring of selective laser melted Ti–6Al–4V parts using Eddy current testing and machine learning. Lect Notes Mech Eng 2024:139–48. https://doi.org/10.1007/978-3-031-47784-3_18.
[140] Tian PQ, Zhan SZ, Feng YW, Zhang XL, Xue XF. Numerical simulation of the reliability of in-situ Eddy current testing considering the influence of penetration depth. IOP Conf Ser Mater Sci Eng 2019;608:1–6. https://doi.org/10.1088/1757-899X/608/1/012001.
[141] Extende. CIVA in a Few Words 2024. https://www.extende.com/civa-in-a-few-words(accessed January 30, 2024).
[142] Nogueira AFL, Weinert RL, Maldonado LJAS. An introductory note on finite element problems based on the Eddy current testing approach. J Electromagn Anal Appl 2021;13:145–59. https://doi.org/10.4236/jemaa.2020.1311011.
[143] Ida N. Eddy current nondestructive evaluation — The challenge of accurate modeling. 2014 Int. Conf. Dev. Appl. Syst., 2014, p. 97–102. doi:https://doi.org/10.1109/DAAS.2014.6842437.
[144] McCann R, Obeidi MA, Hughes C, McCarthy É, Egan DS, Vijayaraghavan RK, et al. In-situ sensing, process monitoring and machine control in laser powder bed fusion: A review. Addit Manuf 2021;45:102058. https://doi.org/10.1016/j.addma.2021.102058.
[145] Scime L, Beuth J. Anomaly detection and classification in a laser powder bed additive manufacturing process using a trained computer vision algorithm. Addit Manuf 2018;19:114–26. https://doi.org/10.1016/j.addma.2017.11.009.
[146] Hamia R, Cordier C, Dolabdjian C. Eddy-current non-destructive testing system for the determination of crack orientation. NDT E Int 2014;61:24–8. https://doi.org/10.1016/j.ndteint.2013.09.005.
[147] Machado MA, Rosado LS, Santos TG. Shaping Eddy currents for non-destructive testing using additive manufactured magnetic substrates. J Nondestruct Eval 2022;41:1–11. https://doi.org/10.1007/s10921-022-00882-1.
[148] EOS. EOS Aluminium AlSi10Mg Material Data Sheet n.d. https://www.eos.info/03_system-related-assets/material-related-contents/metal-materials-and-examples/metal-material-datasheet/aluminium/material_datasheet_eos_aluminium-alsi10mg_en_web.pdf#page=5.08.
[149] Nafiah F, Tokhi MO, Majidnia S, Rudlin J, Zhao Z, Duan F. Pulsed Eddy current: feature extraction enabling in-situ calibration and improved estimation for ferromagnetic application. J Nondestruct Eval 2020:39. https://doi.org/10.1007/s10921-020-00699-w.
[150] Monu MCC, Kumar SS, Brabazon D. Heat treatment of NiTi alloys: influence of volumetric energy density on ageing parameters and the resulting physical properties. J Mater Res Technol 2023;26:9532–55. https://doi.org/10.1016/j.jmrt.2023.09.251.
[151] Monu MCC, Afkham Y, Chekotu JC, Ekoi EJ, Gu H, Teng C, et al. Bi-directional scan pattern effects on residual stresses and distortion in as-built nitinol parts: A trend analysis simulation study. Integr Mater Manuf Innov 2023;12:52–69. https://doi.org/10.1007/s40192-023-00292-9.
[152] Agarwal N, Monu MCC, Tamil Selvam K, Obeidi MA, Brabazon D. Study of the effects of laser power and scanning speed on the microstructural morphologies and physical properties of L-PBF produced Ni52.39Ti47.61. J Mater Res Technol 2023;27:8334–43. https://doi.org/10.1016/j.jmrt.2023.11.146.
[153] Chekotu JC, Groarke R, O'Toole K, Brabazon D. Advances in selective laser melting of nitinol shape memory alloy part production. Materials (Basel) 2019:12. https://doi.org/10.3390/MA12050809.
[154] Chekotu JC, Degli-Alessandrini G, Mughal MZ, Chatterjee S, Goodall R, Kinahan D, et al. Control of mechanical and shape memory characteristics in martensitic NiTi by setting L-PBF parameters and build orientation. J Mater Res Technol 2023;25:6407–31. https://doi.org/10.1016/j.jmrt.2023.07.092.
[155] Chekotu JC, Goodall R, Kinahan D, Brabazon D. Control of Ni-Ti phase structure, solid-state transformation temperatures and enthalpies via control of L-PBF process parameters. Mater Des 2022;218:110715. https://doi.org/10.1016/j.matdes.2022.110715.
[156] Fink A, Fu Z, Körner C. Functional properties and shape memory effect of nitinol manufactured via electron beam powder bed fusion. Materialia 2023;30:101823. https://doi.org/10.1016/j.mtla.2023.101823.
[157] Fink A, Wahlmann B, Körner C. Anisotropic Superelastic and shape memory effect of nitinol manufactured by Electron beam powder bed fusion. Adv Mater Sustain Manuf 2024;1:10004. https://doi.org/10.35534/amsm.2024.10004.
[158] Cao L, Guo W, He B, Li W, Huang X, Zhang Y, et al. In-situ monitoring of the small changes in process parameters with multi-sensor fusion during LPBF. Meas Sci Technol 2024;35:106114. https://doi.org/10.1088/1361-6501/ad5ea5.
[159] Habibalahi A, Moghari MD, Samadian K, Mousavi SS, Safizadeh MS. Improving pulse eddy current and ultrasonic testing stress measurement accuracy using neural network data fusion. IET Sci Meas Technol 2015;9:514–21. https://doi.org/10.1049/iet-smt.2014.0211.
[160] Herzog T, Brandt M, Trinchi A, Sola A, Molotnikov A. Process monitoring and machine learning for defect detection in laser-based metal additive manufacturing. J Intell Manuf 2023. https://doi.org/10.1007/s10845-023-02119-y.